

Exploring Binary Population Evolution in Star Clusters and Testing Stellar Evolution Models

Benjamin A Thompson

August 31, 2012

Contents

1	Introduction	4
1.1	Basic Astrophysics	4
1.1.1	The Magnitude System	4
1.1.2	Filter Systems	5
1.1.3	Color-Magnitude Diagrams + Low-Mass Stellar Evolution	6
1.1.4	Metallicity	10
1.1.5	Interstellar Reddening	10
1.2	Binary Star Systems	11
1.2.1	Visual Binaries	12
1.2.2	Eclipsing Binaries	12
1.2.3	Spectroscopic Binaries	14
1.3	Star Clusters	15
2	Project Overview	16
2.1	Instrumentation and Processing	16
2.1.1	Visual Wavelength Detectors	16
2.1.2	Infrared Wavelength Detectors	17
2.1.3	Image Reduction	17
2.1.4	Magnitude Measurements	18
2.2	Cluster Sample	20
2.3	Available Data	21
2.3.1	Visual Data Sources [0.3 – 1.0 μm]	21
2.3.2	Near-Infrared Data Sources [1.0 – 2.5 μm]	23
2.3.3	Mid-Infrared Data [2.5 – 10 μm]	24
2.3.4	Membership Data	25
2.3.5	Data Overview	25
3	Testing Stellar Evolution Models	25
3.1	Building a Star	26
3.2	Infrared Calibration	27
3.3	Isochrone Fitting	28
3.4	APOGEE	30
3.5	Preliminary Results	30
3.5.1	Comparison	30
3.5.2	Full Cluster Set	31
3.5.3	Membership Cut	31
3.5.4	Empirical Ridgeline	32
3.6	Future Work	35
3.6.1	Additional Systems	35
3.6.2	Separating the Models	36
3.6.3	Binaries	36

4	Binary Cluster Populations and Evolution	36
4.1	Effects of Binary Stars	36
4.1.1	Effect on Stellar Evolution	36
4.1.2	Effect on Cluster Evolution	37
4.2	Current Binary Detection Techniques	38
4.2.1	Two-Band Photometry	38
4.2.2	Radial Velocity Studies	38
4.3	Binary SED Fitting	40
4.4	Code Testing	42
4.4.1	Single Star Test	42
4.4.2	Mass Determination Test	42
4.4.3	Real World Test	42
4.5	Future Work	44

1 Introduction

1.1 Basic Astrophysics

1.1.1 The Magnitude System

Ancient astronomers found it beneficial to classify the stars they observed in the night sky. The Greek astronomer Hipparchus grouped all observable stars into 6 *magnitude* groups: magnitude 1 stars were the brightest, while magnitude 6 stars were the dimmest observable. With the advent of sensitive observing equipment, it was discovered that magnitude 1 stars were 100 times brighter than magnitude 6 stars. From this historical groundwork, the magnitude system was defined: a difference of 5 magnitudes corresponds to a factor of 100 in brightness. With modern telescopes and sensitive observing equipment, astronomers can observe stars that are much dimmer than 6th magnitude, opening up the magnitude scale to high positive magnitudes. The Hubble Space Telescope has a limiting magnitude of roughly 30; stars that are one billionth as bright as what can be seen with the naked eye.

A magnitude increase of 1 corresponds to a brightness difference of $\sqrt[5]{100}$; the magnitude difference between stars will be a logarithm of the ratio of fluxes with a base of $\sqrt[5]{100}$. To determine the difference in magnitudes of two different stars (A and B):

$$m_A - m_B = -\log_{\sqrt[5]{100}} \left(\frac{F_A}{F_B} \right) \quad (1)$$

Converting to more familiar \log_{10} ,

$$m_A - m_B = -\log_{\sqrt[5]{100}} \left(\frac{F_A}{F_B} \right) = -\frac{\log_{10} F_A / F_B}{\log_{10} \sqrt[5]{100}} = -2.5 \log_{10} \left(\frac{F_A}{F_B} \right) \quad (2)$$

Equation (2) defines magnitudes relative to one another, and a zero point is required to complete the scale. There are two different conventions for handling the magnitude scale zero point:

Vega System: Historically, the star Vega was chosen to have a magnitude of 0, with all other stars measured relative to it. Due to uncertainties in flux measurements, however, Vega's magnitude has been refined over time. While the defined zero point of the magnitude scale has stayed the same, Vega now has a magnitude of 0.03. The magnitude of a general star in the Vega system is calculated by:

$$m_{VS} = -2.5 \log_{10} \left(\frac{F}{F_{Vega}} \right) + 0.03 \quad (3)$$

AB System: The zero point of the magnitude scale in the AB system is a flat spectrum. A star in the AB system will have a magnitude:

$$m_{AB} = -2.5 \log_{10}(F_\nu) - 48.6 \quad (4)$$

STMag System: The STmag system, used on space telescopes such as Hubble, is analogous to the AB system, but with flux defined as a function of wavelength instead of frequency. As such, the zero point is different:

$$m_{ST} = -2.5 \log_{10}(F_\lambda) - 21.1 \quad (5)$$

One issue with the magnitude system, as defined by ancient astronomers, is that star brightness is not intrinsic, but correlated with distance from Earth. Light intensity of a star falls off with an inverse square law. In order to compare stars that may be at different distances, the observed magnitudes, called *apparent magnitudes*, are converted to *absolute magnitudes*. The absolute magnitude of the star is its apparent magnitude if it was located at a distance of 10 parsecs (a geometric astronomical distance unit) from Earth.

We compare the apparent magnitudes of a generic star at a distance d (in parsecs) and at a distance of 10 parsecs (denoted by a capital M). Using the fact that flux is $L/4\pi r^2$ (inverse square law), the difference in apparent and absolute magnitude is:

$$m - M = -2.5 \left(\log_{10} \frac{L}{4\pi d^2} - \log_{10} \frac{L}{4\pi (10)^2} \right) \quad (6)$$

The distance dependence is pulled out of the logarithm, and a majority of the equation cancels.

$$m - M = -2.5 \left(\log_{10} \frac{L}{4\pi} - \log_{10} d^2 - \log_{10} \frac{L}{4\pi} + \log_{10} (10)^2 \right) = -2.5 (\log_{10} (10)^2 - \log_{10} d^2) \quad (7)$$

Rearranging and getting rid of exponents gives the absolute magnitude conversion a simple form:

$$m - M = 5 \log_{10} d \text{ (pc)} - 5 \quad (8)$$

Equation (8) is known as the *magnitude-distance relation*. In apparent magnitude, the Sun dominates the scale with an apparent magnitude of -26.7. In absolute magnitude, however, the Sun is a fairly average 5th magnitude star. Getting distances, and therefore absolute magnitudes, allows for inter-comparison of stars anywhere in the Universe.

1.1.2 Filter Systems

Astronomers use photometric filters to allow only specific wavelengths of light into the detector. Broadband filters are created using two panes of glass that are fused together: *cut-on* and *cut-off* layers. The cut-on layer is opaque to short wavelength photons, up to a certain point where it “cuts on” and becomes transparent to longer wavelength photons. The cut-off layer acts oppositely: transparent to short wavelength photons and opaque to long wavelength photons. The combination of these two layers yields a filter where only a small range of wavelengths are able to pass through. By changing the two layers used, filters with the desired wavelength range can be created.

To allow easy comparison of results between telescopes, there are several standard filter systems to which all other measurements are calibrated. Of particular importance to this project are filter systems that cover the visual and infrared portions of the spectrum.

Visual Filters: This project will utilize two sets of standard filters that cover the “visual” range of the electromagnetic spectrum, from 300 – 1000 nm. The first filter systems is called the Johnson-Cousins system, consisting of five filters, *UBVRI* (Bessell 1990). Alternatively, there is the Sloan filter system, *ugriz* (Fukugita et al. 1996). Both visual filter systems provide near

seamless coverage between 300 – 900 nm, illustrated in figure 1.

Near-IR Filters: The 1.0 – 2.5 μm wavelength range is covered by three near-infrared filters that comprise the 2-Micron All Sky Survey (2MASS) (Skrutskie et al. 2006) filter system, JHK_S . Unlike the visual systems, 2MASS filters do not provide uniform coverage throughout this range. The gaps between the filters, at 1.4 and 1.9 μm , correspond to regions of absorption from water vapor and CO_2 in the atmosphere. These spectral regions would not provide any photons from the star, so the 2MASS filters were designed to avoid sky contamination in these regions.

Mid-IR Filters: Beyond 2.5 μm , absorption from the Earth’s atmosphere becomes so strong that few photons will reach the surface. To overcome this, mid-infrared observations are usually taken from space. The mid-IR standard filter system used in this project, [3.6][4.5][5.8][8.0] are from the Infrared Array Camera (IRAC) on the *Spitzer* Space Telescope (Fazio et al. 2004).

Table 1 lists the filters that will be used in this project along with the central wavelengths and approximate width of the transparent region.

Table 1: Central wavelengths and effective widths of all filters used in this project.

System	Filter	Central λ (nm)	Width (nm)
Johnson-Cousins	U	365	66
	B	445	94
	V	551	88
	R	658	138
	I	806	149
Sloan	u	350	57
	g	480	137
	r	625	137
	i	770	153
	z	910	95
2MASS	J	1235	162
	H	1662	251
	K_S	2159	262
IRAC	[3.6]	3567	776
	[4.5]	4485	1060
	[5.8]	5729	1427
	[8.0]	7893	2901

1.1.3 Color-Magnitude Diagrams + Low-Mass Stellar Evolution

Stars go through a variety of stages during their lifetime, and the easiest way to visualize stellar evolution is through the use of a *Hertzsprung-Russell* (H-R) diagram. A H-R diagram plots stars with Luminosity on the y-axis, and Temperature on the x-axis. While a H-R diagram is the easiest way to visualize stars, neither Luminosity nor Temperature is an observed quantity. Instead, we create *color-magnitude* diagrams (CMDs), which plot a filter magnitude on the y-axis and a *color*

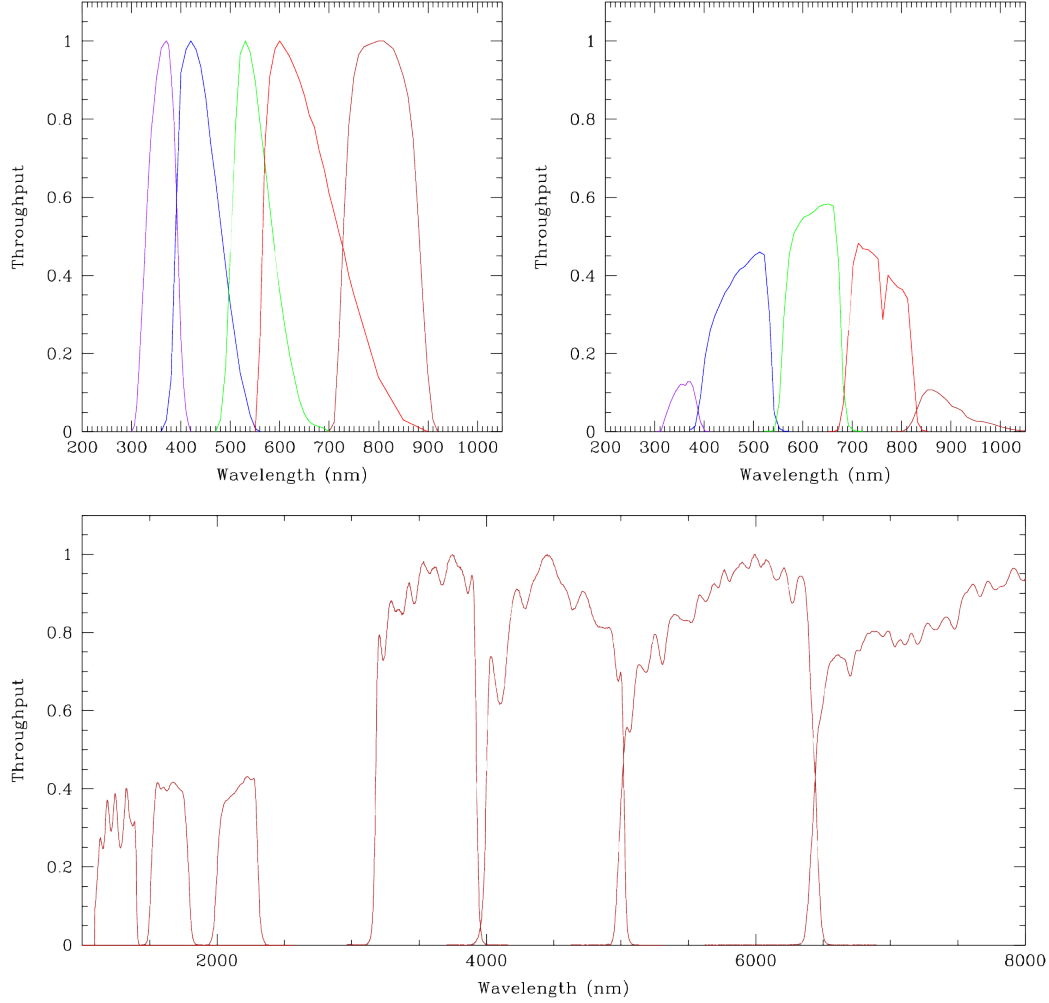


Figure 1: Effective ranges of all filters used in this paper. (*Top Left*) Johnson Filters: *UBVRI*. (*Top Right*) SDSS Filters: *ugriz*. (*Bottom*) 2MASS + IRAC filters: *JHK_S[3.6][4.5][5.8][8.0]*.

on the x-axis. A color is calculated by subtracting the magnitude of a star in a higher wavelength filter from the star's magnitude in a lower magnitude filter, e.g. $B - V$ or $V - K$.

CMDs are much easier to create, due to the fact that no other information about the stars need to be known besides their observed magnitude. If other information is known, it is possible to convert a CMD into a H-R diagram. Equation (8), along with stellar models, can be used to convert a filter magnitude to an absolute magnitude and then to a luminosity. A color is related to temperature due to the fact that bluer (hotter) stars will have a negative color, while a red star (cooler) will have a positive color. Using known relations, colors of stars can be transformed into temperatures, if needed.

While H-R diagrams can be plotted for any collection of stars, CMDs are usually created for star clusters (to be discussed later in section 1.3). A CMD of Hubble Space Telescope data for a

cluster is plotted in figure 2. Stages of stellar evolution are labeled 1 through 5. The list below explains what changes the star is experiencing during each stage of evolution.

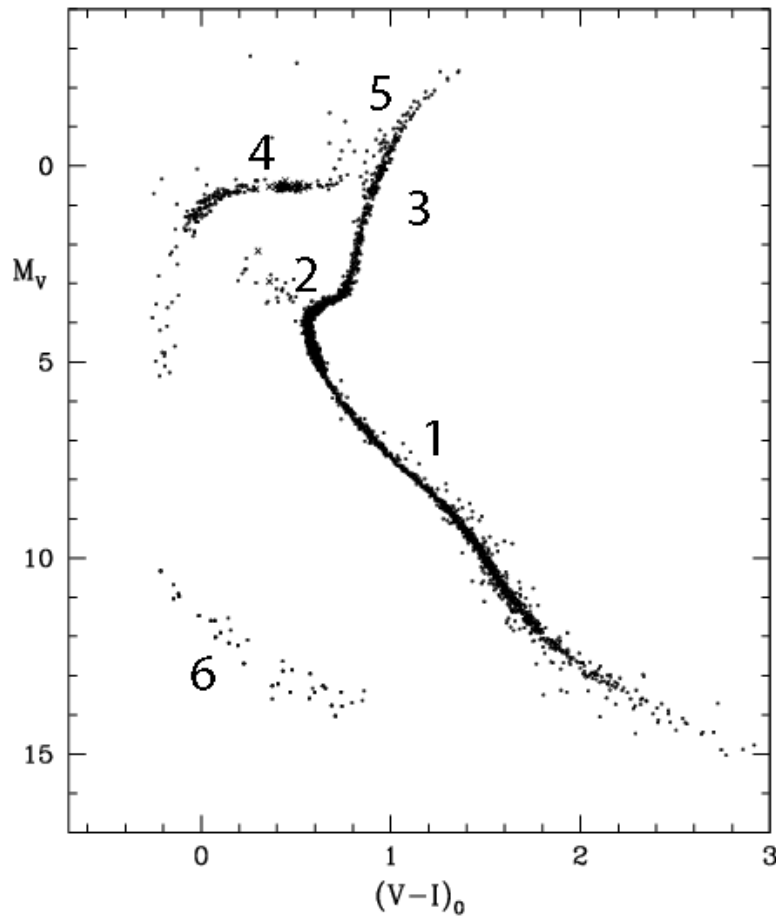


Figure 2: Hubble Space Telescope CMD for a globular cluster. Evolutionary stages are labeled.

1. **The Main Sequence (MS):** A star is born the moment its core begins to fuse Hydrogen into Helium. For a majority of its life, Hydrogen to Helium conversion in the core is the star's main source of energy. During this phase, the star is located on a region of the CMD called the *main sequence*. Larger mass stars are brighter and hotter than lower mass ones, and are therefore located at the top of the MS. As the hydrogen fuel in its core begins to become depleted, a star cools slightly, moving right on the CMD. For the most part, however, MS stars are located on a straight line.
2. **Turnoff + Subgiant branch:** When Hydrogen in the star's core becomes depleted, it can no longer create enough energy to sustain the weight of the layers above it, and the core begins to collapse. These stars have completed their time on the main sequence, and can be seen on the CMD at the *turnoff point*. As the core collapses and releases gravitational energy,

a shell of Hydrogen around the core begins to heat until Hydrogen fusion begins in the shell. As the shell has more volume than the core below it, the increased energy output expands the outer layers of the star, cooling it and increasing its brightness as it moves through the *subgiant branch*. During this phase and the next, the Hydrogen-depleted core remains inert.

3. **Red Giant Branch (RGB):** As the shell continues to convert Hydrogen to Helium, the stellar atmosphere opacity increases due to the decrease in temperature and, thus, increase in H^- ions. This opacity increase leads to convection becoming the most efficient energy transport method and convection cells forming near the surface. The increase in energy transport efficiency leads to an increase in luminosity as well as causing the outer layers of the star to expand again. This expansion causes the temperature to decrease even more, and the entire cycle repeats. This continues to happen as the shell consumes its Hydrogen fuel.

As stars near the tip of the RGB, they become so large that their outer layers may be blown off by stellar winds. While not all stars experience mass loss during their ascent of the RGB, the mass loss rates for some stars can be substantial. At the tip of the RGB, the shell runs out of Hydrogen fuel and the entire star begins to contract.

4. **Horizontal Branch (HB):** As the star contracts, the temperature increases and the core of the star begins to fuse Helium into heavier elements. The *horizontal branch* evolutionary phase is a Helium analogue of the Hydrogen main sequence. The star remains almost stationary on the CMD as it converts all of the Helium within the core. As there is much less Helium within the star than Hydrogen, the timescale of the horizontal branch is much less than that of other evolutionary phases.

There are two distinct halves of the horizontal branch, a red and blue section (visible in figure 2). The difference between these sections is not completely understood, but is thought to be related to the mass loss of the star along the RGB. If the outer layers of the star are lost near the tip of the RGB, we are observing further into the star than if there was no mass loss, leading to a higher observed temperature and bluer color.

5. **Asymptotic Giant Branch (AGB):** As the HB is an analogue of the MS, the AGB is the Helium analogue of the RGB. Named because it approaches the RGB asymptotically from the left of the CMD, the AGB contains stars that are burning Helium in a shell around the core and are at least partly convective.
6. **Post AGB Evolution:** While a star is on the AGB, it experiences a high rate of mass loss. Strong stellar winds continue after the star reaches the tip of the AGB, blowing off most of the star's outer cooler layers, leaving only the hotter inner regions. Since the star's Helium shell continues burning, the luminosity stays the same. This results in the star tracking blueward at the top of the CMD. When only a small layer of material remains on top of the Helium burning shell, the temperature drops rapidly and the fusion stops. The star's luminosity drops rapidly, and the star ends its life as a white dwarf on the bottom left of the CMD.

The AGB to white dwarf transition only happens for medium to low mass stars, less than $8 M_{\odot}$. Higher mass stars will end their lives in supernovae explosions, ending as either a neutron star or black hole. The transition to these stellar remnants is beyond the scope of this paper.

1.1.4 Metallicity

A star’s *metallicity* is an important quantity when determining its properties. Astronomers consider anything besides Hydrogen and Helium to be “metals”. Metallicity is the fraction of atoms within a star that are metals, and is often denoted by the letter Z . The Sun has a metallicity of $Z = 0.0188$, meaning that slightly less than 2 of every 100 atoms within the Sun are something heavier than Helium. While denoting a star’s metallicity using Z is fairly common, it can also be expressed in terms of dex, which is the log of the ratio of the star’s Z to the Sun’s. Given a metallicity of N dex, Z can be found using:

$$Z_{star} = Z_{\odot} \times 10^{N \text{ dex}} \quad (9)$$

While the term metallicity is most often used to describe the overall metal content of the star, metallicity can also refer to the abundance of particular elements within the star. Usually the ratios of these elements are consistent, but sometimes anomalous stars will be observed with certain elements far more abundant than predicted. Individual elemental abundances are calculated as ratios of that element to Hydrogen, and then calibrated to the Sun’s value (similar to the dex definition). For iron, its abundance is written as $[\text{Fe}/\text{H}]$ and calculated by:

$$[\text{Fe}/\text{H}] = \log \frac{(N_{\text{Fe}}/N_{\text{H}})_{\text{Star}}}{(N_{\text{Fe}}/N_{\text{H}})_{\odot}} \quad (10)$$

Metallicity measurements will not be the focus of this project, and any metallicity information used in the analysis will be gathered from outside sources. Metallicity information will be extracted from a high-quality and uniform dataset, described in section 3.4

1.1.5 Interstellar Reddening

Interstellar space contains gas and dust that scatters and absorbs star photons. The scattering of light by interstellar gas causes two related effects: *extinction* due to the fact that photons being absorbed or scattered by gas means that the star will appear dimmer than it actually is, and *reddening* due to the fact that shorter (bluer) wavelengths are scattered more than longer wavelengths, altering the color of the star so that is measured to be redder than it actually is.

Extinction is denoted using the term A_X , where X is the specific band you are interested in, and is calculated using:

$$A_X = (M_X)_{\text{intrinsic}} - (M_X)_{\text{observed}} \quad (11)$$

Extinction adds another term to equation (8), converting the magnitude-distance relation to:

$$m_X - M_X = 5 \log_{10} d - 5 + A_X \quad (12)$$

Reddening for a given color, say $B - V$, is denoted by the value $E(B - V)$:

$$E(B - V) = (B - V)_{\text{intrinsic}} - (B - V)_{\text{observed}} = A_B - A_V \quad (13)$$

Extinction and reddening are intertwined effects, as seen in equation (13), and have been related experimentally. This is done by comparing spectra of two stars of the same spectral type: one which is not reddened, and the other which is observed through dust. The stars are assumed

to have similar physical properties, but the flux from the reddened star will be less than that from the non-reddened one.

It was found that galactic extinction curves (extinction vs wavelength) could be approximated by an analytic function with a single variable: $R_V = A_V/E(B-V)$, the total-to-selective extinction ratio (Cardelli et al. 1989). Extinction curves with a range of R_V values are plotted in figure 3.

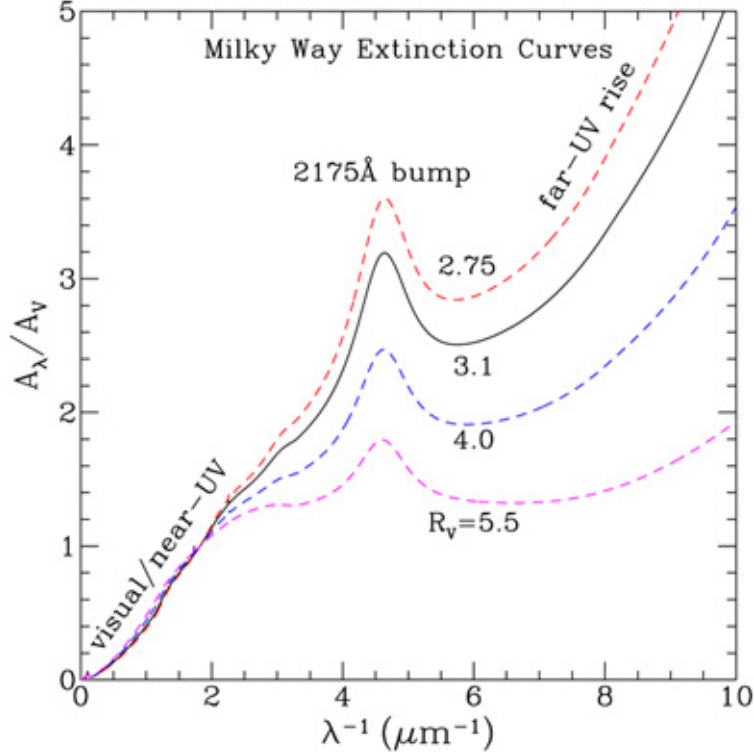


Figure 3: Extinction curves for the Milky Way for a variety of R_V values.

Extinction curves are governed by the overall distribution of dust grain sizes. For regions with larger percentages of small grain dust, R_V is decreased, leading to a larger 2175 Å bump and steeper far-UV slope. For the spectral region this project is concerned with (300 nm - 10 μm), the extinction curve does not depend heavily on R_V . For all analyses, we will assume the galactic average, $R_V = 3.1$. Extinction values for visual and near-IR filters used in the project are listed below in table 2

1.2 Binary Star Systems

Binary star systems, or sometimes *binary stars*, are a system of two stars orbiting a common center of mass. The more massive star in the system is called the *primary* star while the smaller is called the *secondary*, or companion, star. There are several classifications of binary systems, characterized by how each is observed. An overview of each type of system is included below, along with an explanation of any relevant information that can be gained from each.

Table 2: Extinction Relations in Relevant Filters

Filter	A_X/A_V	Source
U	1.531	Binney & Merrifield (1998)
B	1.324	
V	1.000	
R	0.748	
I	0.482	
u	1.593	Fan (1999)
g	1.199	
r	0.858	
i	0.639	
z	0.459	
J	0.282	Binney & Merrifield (1998)
H	0.175	
K_S	0.112	

1.2.1 Visual Binaries

If a binary is close enough to Earth and the separation between stars in the system is great enough, both stars in the system can be individually resolved by telescopes. The star Castor in the constellation Gemini is an example of this type of system, called a *visual binary*. The system can be observed throughout an entire orbital period, or an appreciable portion of one, so the shapes of each star's orbit can be determined. Using this information, the masses of each star can be determined. By measuring the light from each star, astronomers can determine the temperature and spectral type of the two members. Visual binaries are extremely important to much of astronomical understanding due to the large number of system parameters that can be determined observationally.

1.2.2 Eclipsing Binaries

Similar to lunar and solar eclipses that are witnessed on Earth, a binary system can have eclipses where one of the stars passes in front of the other along the line of sight from Earth. A diagram of an eclipsing binary system, along with a plot of observed brightness over time is shown in figure 4. For this example, the smaller star is assumed to be hotter: a main sequence star with a red giant companion.

The first quantity that can be easily measured from an eclipsing binary is the ratio of temperatures of each star. At each point in the orbit, the flux from the system is measured (right panel of figure 4). When both stars are visible, the flux from the system is

$$B_0 = k (\pi r_L^2 F_L + \pi r_S^2 F_S) \quad (14)$$

Here, L corresponds to the larger star, and S to the smaller star. The parameter k is a multiplicative factor that accounts for the distance to the system as well as the filters and optics that are used for the measurement. When the smaller star is between positions b and c in figure 4, only the large star is visible, making the measured flux:

$$B_{bc} = k (\pi r_L^2 F_L) \quad (15)$$

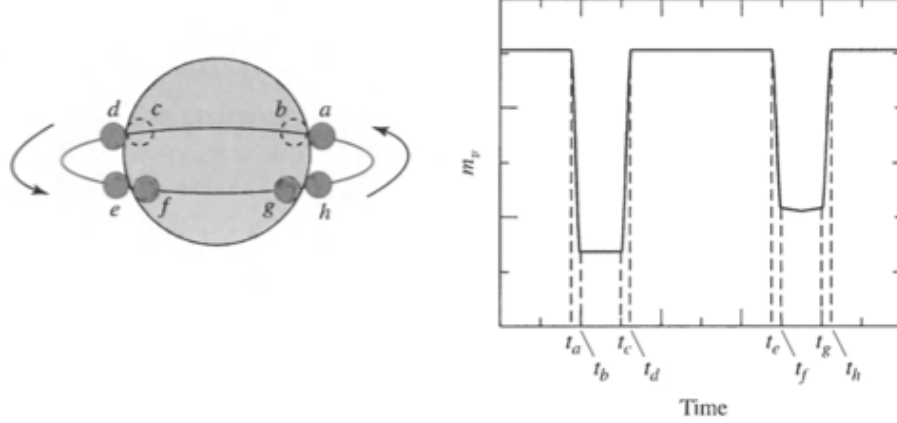


Figure 4: Light curve of an eclipsing binary system. Times denoted on the light curve correspond to the star positions on the left. Figure reproduced from Carroll & Ostlie (2006)

The final configuration of the eclipsing system happens when the smaller star is between positions f and g. Then the total flux is:

$$B_{fg} = k [(\pi r_L^2 - \pi r_S^2) F_L + \pi r_S^2 F_S] \quad (16)$$

Combining these equations and utilizing the Stefan-Boltzmann equation $F = \sigma T^4$, we find:

$$\frac{B_0 - B_{bc}}{B_0 - B_{fg}} = \frac{F_S}{F_L} = \left(\frac{T_S}{T_L} \right)^4 \quad (17)$$

Using the observed quantities (fluxes at specific points in the orbit), we can deduce the ratio of temperatures of the two stars, which is helpful in determining the spectral types of the two stars and understanding the mechanics of the binary system.

If the velocities of the stars in the system are known (which is possible using techniques described in the next section), it is also possible to deduce the radii of the individual component stars in the system. Below, it is assumed that stars have a constant speed over the regions we are interested in, but these equations can be modified if there are appreciable changes in velocity as well. The radius of the each star is computed, where v is the relative velocity of the two stars:

$$r_S = \frac{v}{2} (t_b - t_a) \quad (18)$$

$$r_L = \frac{v}{2} (t_c - t_a) \quad (19)$$

Being able to determine temperatures and radii of stars allow for an easy determination of each stars' spectral type and evolutionary stage, which is helpful in understanding the internal mechanics of the binary system.

While the above two types of binary systems are important due to the wealth of information that can be gained, they are also quite rare. The linear resolution of a telescope falls off with

distance, so any visual binaries detected must be fairly close to Earth. Binaries can also be formed in almost any orientation; their plane of orbit may be at any angle with respect to our line of sight, called *inclination*. Only for binaries with an inclination of almost 90° will Earth observers see eclipses, and therefore eclipsing binaries are extremely rare. To study binaries in a wide range of environments, more than visual and eclipsing binary systems will be needed.

1.2.3 Spectroscopic Binaries

If a star is moving along the line of sight from Earth, its light is shifted due to the Doppler effect. Observed spectral lines will be blue- or red-shifted depending on the star's velocity. By comparing the observed spectral lines from a star to known wavelengths, the speed of the star can be determined, which is called a *radial velocity*. Single stars will have roughly a constant radial velocity throughout a short period of time (hundreds of days), while many binary systems will show systematic shifts in radial velocity as the stars orbit each other.

If both stars in the binary system are of comparable luminosity, spectral lines from both stars can be observed. These *double-lined binaries* allow for an estimation of the masses of both stars in the system as well as an understanding of the orbits of each star. Using the velocity of each star, as well as the orbital period, the semi-major axis of the system can be calculated.

$$a = a_1 + a_2 = \frac{P}{2\pi v_1} + \frac{P}{2\pi v_2} \quad (20)$$

Plugging this into Kepler's 3rd law and solving for the mass of the individual stars gives,

$$m_1 + m_2 = \frac{P}{2\pi G} (v_1 + v_2)^3 \quad (21)$$

Radial velocities from spectroscopic binaries are complicated due to the inclination angle, i , of the system. If the orbit of the system is angled with respect to the line of sight from Earth, the radial velocity measured will be less than the orbital velocity of the system by a factor of $\sin i$ (illustrated in figure 5). Adding this to equation (21),

$$m_1 + m_2 = \frac{P}{2\pi G} \frac{(v_{1r} + v_{2r})^3}{\sin^3 i} \quad (22)$$

Here v_{1r} and v_{2r} are the actual radial velocities measured by astronomers. This equation gives upper bounds on the possible masses of the stars in the system, but cannot exactly determine them due to the uncertain inclination. Information can also be gained from *single-lined binaries*, where one of the companions is too dim to be observed in the spectra. We replace the ratio of radial velocities by the ratio of masses to obtain the formula,

$$\frac{m_2^3}{(m_1 + m_2)^2} \sin^3 i = \frac{P}{2\pi G} v_{1r}^3 \quad (23)$$

The right hand side of equation (23) is called the *mass function*, and only depends on observable quantities: the period and primary star radial velocity. Although the individual masses of the stars cannot be determined with only one star's velocity information, it does give a lower bound for m_2

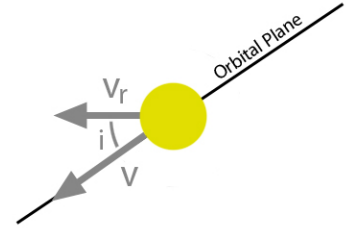


Figure 5: Difference between true velocity v and observed velocity v_r when orbit has inclination angle i .

since the left hand side of equation (23) is always less than m_2 . Single-lined binaries, however, are only useful for statistical studies and not for determining the mechanics of the system itself.

The above classifications are not mutually exclusive. A spectroscopic binary may have an inclination of 90° and therefore also experience eclipses. Such a system is called an *eclipsing spectroscopic binary*. These systems are useful, as the inclination is removed from the equations above. Double-line eclipsing spectroscopic binaries allow for the determination of the masses of both stars as well as the period and eccentricity of each star’s orbit.

Large-scale binary detection techniques will be expanded on later, in section 4.2.

1.3 Star Clusters

Of all the parameters that determine the observable properties of a star, age is the hardest to determine. Metallicity can be measured through spectroscopy, distance can be found using parallax (for close stars), but determining the age of a single star is near-impossible. The Sun, the star we know the most about, is dated through radioactive dating analyses of meteorites instead of through direct measurements. Using star clusters instead of individual stars, however, allows for accurate age determination of all member stars. Due to this fact, star clusters are excellent tracers of galactic evolution as their properties can be correlated accurately with age.

A star cluster is a gravitationally-bound collection of stars that formed from the same large cloud of interstellar gas at roughly the same time. By this definition, cluster stars are assumed to have a common age and homogeneous chemical composition. A cluster’s distance from Earth is usually much larger than the size of the cluster, and therefore it can be assumed all stars are at the same distance. It is also assumed that all stars within a cluster have their light pass through the same line of sight to Earth. Any gas clouds that redden the light from one star in the cluster will have the same effect on all stars in the cluster. While field stars will have varying values of metallicity, age, distance and reddening, star clusters will have a single set of parameters for all stars.

Recent studies have shown that the assumption of homogeneous populations to be false for some clusters. Several globular clusters show multiple stellar populations (Piotto et al. 2007), and recently has been seen in an open cluster as well (Geisler et al. 2012). It is possible that the explosions of first generation massive stars in a cluster caused another round of star formation. This second generation of stars will not only be younger than the first generation, but the “pollution” of the interstellar medium by supernovae remnants will cause the metallicity to change as well. These *multiple starburst* clusters are harder to study, as it cannot be assumed that the cluster can be modelled using a single age and metallicity. Additionally, there are clusters that experience *differential reddening*, where reddening throughout the cluster is not constant, but for the most part this assumption holds.

Star clusters come in two forms: globular and open clusters.

Globular clusters are dense collections of 10,000 to a few million stars. Globular clusters are usually very old, around 13 Gyr (for reference, the Universe is 13.7 Gyr old), and have a large metallicity spread (~ 1.5 dex). Globular clusters are distributed roughly symmetrically around the galactic center (or centers of other galaxies) and have highly eccentric orbits, usually at an angle from the galactic plane. The Milky Way has roughly 150 globular clusters, while the nearby Andromeda Galaxy may have as many as 500 (Barmby & Huchra 2001).

Open clusters are loose collections of a few hundred to a few thousand stars all formed from the same interstellar gas cloud within the galactic disk. In distinction to globulars, open clusters are found within the disk of the galaxy and are usually significantly younger and more metal-rich. Over 1000 open clusters have been discovered, and many more are thought to exist.

We are most interested in the evolution of the cluster environment, and as such, open clusters provide the best possible insight. Open cluster ages range from still-forming to around 10 Gyr, while globular clusters are all roughly 13 Gyr old. Using open clusters allows for stepping through the evolutionary process while globular clusters only provide a “snapshot” of cluster characteristics for very old populations.

2 Project Overview

Through this project we aim to answer several questions:

1. *Which stellar evolution model is most accurate?* The process of stellar evolution is still not completely understood, and several evolution models have been published. These models will be compared to our clean stellar samples for a cluster sample with a variety of ages and metallicities in order to determine which model works best. Finding where these models match observations, and where they fail, will give insight into the underlying physics.
2. *What is the binary fraction in star clusters and how does it vary as a function of primary star mass?* The formation of binaries stars in a clustered environment is difficult to study due to the different formation time scales. By studying clusters of different ages, we will be able to constrain the “initial” binary population, needed for cluster simulations. We will also determine whether mass ratio is dependent on primary star mass, which will provide additional insight into mechanisms of binary formation.
3. *How does the binary population affect stellar and cluster evolution?* Creation processes for non-standard stars such as blue stragglers and sub-subgiants are hypothesized to involve a binary system. Directly comparing binary fraction to non-standard star frequency for multiple clusters will allow testing of these formation models. Our binary results will also be directly compared to N-body models of cluster evolution in order to observe the binary population’s effects on cluster evolution and destruction.

The rest of this section will discuss the instruments, cluster sample and data to be used in this project. Section 3 will discuss testing of stellar evolution models, called isochrones, to this cluster sample. Section 4 will use these stellar models to identify and characterize low-mass binary systems.

2.1 Instrumentation and Processing

2.1.1 Visual Wavelength Detectors

Astronomy was ushered into a new era in 1979 when the first charge-coupled device (CCD) detector was installed on the 1-meter telescope at Kitt Peak National Observatory. Before this, photographic

plates had been the standard, but the new CCD cameras were much more efficient, allowing the detection of fainter objects than even the best photographic plates.

A CCD detector is an array of individual CCDs that make up the pixels of the camera. CCDs use a layer of silicon as the main optical element, so when a photon strikes the silicon, an electron is excited to the conduction band and transferred to a “gate” where the charge is stored. When an image is ready to be read out, the first row in the array dumps its charge into a charge amplifier, converts that charge to a voltage, and stores that voltage as a numerical value for that pixel. Once the first row is completely converted, an electric field is applied to transfer the charge from the second row into the first, where it is then read out. This process continues until all rows of the chip have been counted.

Silicon has a band gap height of roughly 1.0 eV, depending on temperature. This corresponds to a photon with a wavelength of 1240 nm, around the location of the J filter. Photons with wavelengths greater than this (most of the infrared range) will not be able to excite an electron to the conduction band, and therefore different types of detectors must be used for infrared filters.

2.1.2 Infrared Wavelength Detectors

IR detectors function similarly to CCDs. A semiconductor is struck by a photon, exciting it to the conduction band and transferring the charge. Instead of storing the charge in a gate and reading out all pixels at the end of an exposure, each pixel of a IR detector has its own readout amplifier. As charge accumulates, the amplifier keeps track of the accumulated voltage, and results can be accessed and stored when required. Reads of the chip are *non-destructive*, meaning that the accumulated charge is not altered by measuring a pixel’s value, much different than for a CCD. IR detectors allow for reading out only parts of a chip, or reading out a chip multiple times throughout an exposure.

There are several different types of semiconductors used in IR detectors. Mercury cadmium telluride (HgCdTe) detectors have a band gap of 0.5 eV, corresponding to a limiting photon wavelength of 2500 nm, making them ideal for near-IR studies. Another choice is indium antimonide (InSb) which has a band gap of 0.25 eV (5000 nm), allowing for use in the near- and part of mid-IR range. For further mid-IR filters, silicon arsenide (SiAs) detectors are ideal due to their very small band gap of 48 meV (25 μm).

2.1.3 Image Reduction

To prepare a science image for analysis, the following corrections must first be made to account for a variety of instrumental effects. As CCDs and IR detectors function differently, each correction will be labelled with the type(s) of detectors it needs to be applied to.

Bias Correction [CCD]: To transfer charge between rows in a CCD, an electric field is applied. The energy stored in this electric field may cause extra electrons to be excited as the charge migrates across the chip. These extra electrons are not part of the signal, and must be corrected out. To remove them, the chip is read out multiple times in succession without exposing. These “0 second” images will show no counts besides those from the charge transfer process. Bias frame counts are subtracted from all images.

Dark Current [CCD, IR]: The detector is usually cooled to liquid nitrogen temperatures, but this still leaves some thermal energy that can excite an electron within the detector to the conduction band. Additionally, there may be defects on the chip that cause some pixels to register large counts regardless of where they are pointed, called *hot pixels*.

To correct for this, an image is taken with the shutter closed. Because no light from the sky hits the chip, all the detected counts are from the electronics themselves. Averaging several of these *dark frames*, and subtracting bias counts, will determine the average thermal excitation counts for each pixel as well as other electronic defects. Dark frames are subtracted from all images.

Flat Fielding [CCD, IR]: When a photon strikes a pixel of the detector, an electron will not always be excited and recorded for that pixel. The percent chance that an incoming photon will register a count with the detector is called the *quantum efficiency*. The quantum efficiency of a detector is usually above 90%, but it is not always the same for each pixel. In addition, the filter being used may not be manufactured perfectly or there may be dust grains lying on the various surfaces of the telescope. Imperfections of the filter may cause light to be refracted in unintended ways, limiting the effectiveness of certain pixels on the chip. This effect is lumped into each pixels' overall efficiency.

Correcting for this effect can be accomplished in two ways. First, the telescope can be pointed at a flat surface that is uniformly lit by a lamp, or multiple lamps. The resulting image, called a *flat field*, should have identical counts for all pixels, but due to the non-uniform efficiency, some pixels will register fewer counts.

The lamps used for flat-fielding have a specific temperature, so the flux through some filters may not be very high (for example, *U* and *B* filters). Instead of using the lamps, the telescope is pointed at several different points in the sky and images are taken. If the images are taken high enough in the sky, away from high light pollution areas near the horizon, the photon counts from the sky should be roughly constant. Combining these multiple images using a median will create a *sky flat*, removing any stars in the frames and leaving only a sky background. Similar to the flat field image, this sky flat should be uniform, but some pixels will register fewer counts due to lowered efficiency.

Once the flat image is taken (be it a flat field or sky flat), the bias and dark frame are subtracted (to remove electronic effects), and it is then normalized. In the normalized image, each pixel's value represents its efficiency. The science image counts are divided by the normalized flat field to bring all pixels to the same effective level. Analogous to dark frames, which correct for effects from the electronics, flat fielding corrects for effects within the optical elements of the system.

2.1.4 Magnitude Measurements

Measuring star brightnesses, and then magnitudes, from images is accomplished through a process called *photometry*. There are two different approaches to photometry, described below.

Aperture Photometry: This technique uses three circles, called apertures, to determine the number of photons from a star. The setup of the three apertures for a fictional star is shown in figure 6. The innermost circle, called the *image circle*, is centered on the star and has a radius such that it encloses the entire image of the star. The number of photon counts within this circle come from two effects: photons coming from the star itself, as well as photons from the sky background.

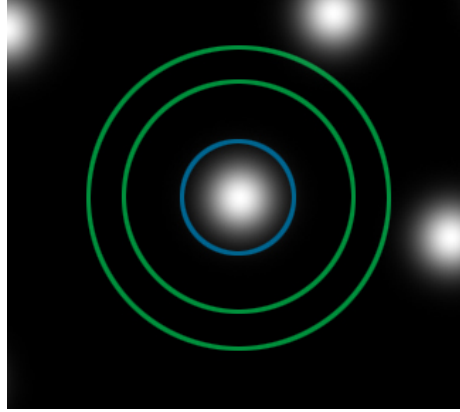


Figure 6: Aperture photometry set-up for a fictional star. Blue is image circle, green indicates sky annulus. As can be seen, if stars were any closer together one might fall within sky annulus.

To remove these sky photons, the next two circles are used to form a ring, called the *sky annulus*. The counts within the sky annulus are assumed to all come from the sky background, and is used to determine the average number of sky photons per pixel in the image. Using this information, the sky photon counts can be removed from the image circle, leaving only a count of photons from the star.

The benefit of this technique is that it is simple to do and fast to compute. The only input parameters are the three circle radii, and a computer can determine magnitudes for thousands of stars very quickly. The breakdown of this technique, however, happens when stars are close together. If another star falls within the sky annulus, the assumption that all counts from the sky annulus are from background sources will not be valid. For sparse fields, aperture photometry is the most efficient way to determine magnitudes.

PSF Photometry: Diffraction due to light passing through the aperture of the telescope produces a pattern called an *Airy disk*. Point-source function (PSF) photometry measures the magnitude of a star by fitting a mathematical function (Gaussian / Lorentzian) to the Airy disk, then integrating over it to find the total photon counts. Figure 7 shows an example of a PSF fitting. In both cases, the sky background is roughly 100 counts, setting the baseline of the gaussian fit function. The power of PSF photometry is shown in the right hand panel of figure 7, where two stars in the frame partially overlap. Aperture photometry can not handle crowded fields, but PSF fittings are able to separate partially overlapping brightness profiles, allowing accurate magnitudes in dense environments. This approach is especially useful for clusters, where the density of stars is higher than in the field.

PSF fitting is more computationally difficult than aperture photometry, as the parameters of the fit (e.g. σ for a gaussian) may change with position on the chip. However, these extra parameters allow for more accurate fits of the data and can produce more reliable results. The PSF photometry in this project was completed using the program DAOPHOT II (Stetson 1987). DAOPHOT allows variation PSF parameters linearly or quadratically across the chip, as well as

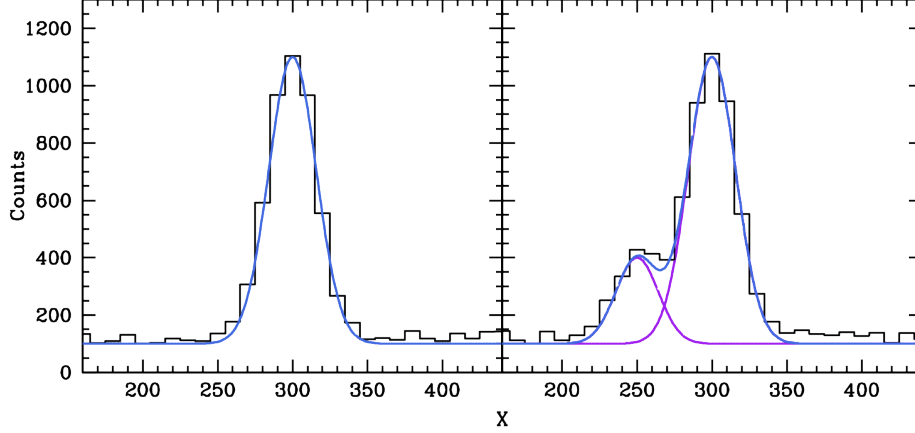


Figure 7: Brightness profiles along a single row of a chip. *Left:* Gaussian fitting to a single star, sky background of ~ 100 counts. *Right:* Gaussian fitting of two overlapping stars, sky background of ~ 100 counts. Blue curve is sum of both purple individual star gaussian fits.

the option to use a gaussian, lorentzian, or sum of both as the shape for the PSF. A majority of the data in this project is derived using PSF photometry.

2.2 Cluster Sample

Open clusters for this project were chosen as part of the WIYN Open Cluster Survey (WOCS), a broad collaboration of roughly 15 astronomers and their students dedicated to providing a comprehensive study of a select set of open clusters. WOCS is utilizing photometry, astrometry, spectroscopy and theory to expand the number of open clusters that provide a foundation for stellar astrophysics. Some of the clusters chosen for this project already have high quality RV studies with which to compare our binary results.

In total, 18 WOCS clusters will be analyzed using our techniques. The distribution of cluster parameters for our sample is shown in figure 8. Ages range from 25 Myr to 9 Gyr while $[\text{Fe}/\text{H}]$ varies from -0.38 to $+0.32$ — 40% to 200% the Iron content of the Sun.

Of the 18 total clusters, five currently have complete data sets and will comprise much of the preliminary results. Descriptions and parameters of these clusters are listed below.

NGC2168 [M35] (100 Myr, $[\text{Fe}/\text{H}] = -0.16$): The young cluster M35 provides an excellent starting point for cluster evolution. Additionally, M35 is one of four clusters that have detailed companion RV-based WOCS binary studies (Geller et al. 2010), and will allow for checks of binary results. Another cluster in the sample, M37, has a similar age (350 Myr), but different chemistry ($[\text{Fe}/\text{H}] = +0.09$). Comparison of results between M35 and M37 will allow us to explore environmental effects on “initial” binary population.

IC 4651 (1.1 Gyr, -0.1 dex): A mid-point in the cluster evolution sequence, IC 4651 provides a check on N-body simulations of early cluster evolution.

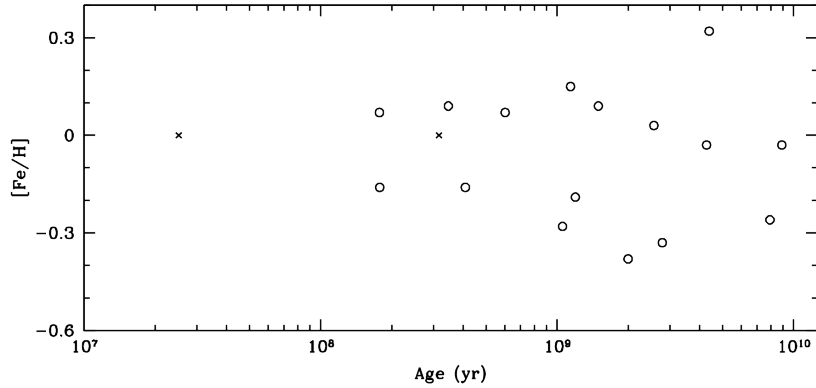


Figure 8: Distribution of 18 project clusters in age and metallicity, $[\text{Fe}/\text{H}]$. X's represent clusters which do not have any published metallicity information. (Dias et al. 2002)

NGC 2682 [M67] (4.3 Gyr, +0.0 dex): The cluster M67 is the one of the most fundamental in the basis of stellar astrophysics due to its age and chemistry that are nearly identical to the Sun. As an important open cluster, some stellar evolution models have been calibrated to M67 (VandenBerg et al. 2006). Comparing these models to those calibrated on globular clusters may illuminate physical differences between the two types.

NGC 188 (7 Gyr, -0.01 dex): NGC 188 is the most studied WOCS cluster with photometry, astrometry and RV-based binary studies (Geller et al. 2008, von Hippel & Sarajedini 1998), making it an ideal candidate for preliminary work.

Collinder 261 (9 Gyr, -0.14 dex): Being one of the oldest open clusters in the Galaxy, Collinder 261 is the “end” of cluster dynamical evolution in the Milky Way Disk. Results from NGC 188 can be compared to those from Collinder 261 in order to understand metallicity’s effect on the final stages of cluster evolution (analogous to M35/M37 on the young end).

2.3 Available Data

Data that will be used in this project were compiled from a number of sources.

2.3.1 Visual Data Sources [0.3 – 1.0 μm]

Sloan Digital Sky Survey (SDSS): Beginning operations in 2000, the SDSS Legacy Survey aimed to provide uniform and well-calibrated photometry for much of the northern sky. Observations were taken using the SDSS 2.5m telescope at Apache Point Observatory (APO) in the Sacramento Mountains of New Mexico. To efficiently cover large contiguous areas of sky, SDSS observations were taken using a technique called *drift scanning*. In drift scanning, the telescope is kept stationary as the stars move horizontally across the chip over time. The CCD chip is read out at exactly the same speed as the stars move across a single pixel, allowing for the electrons from a

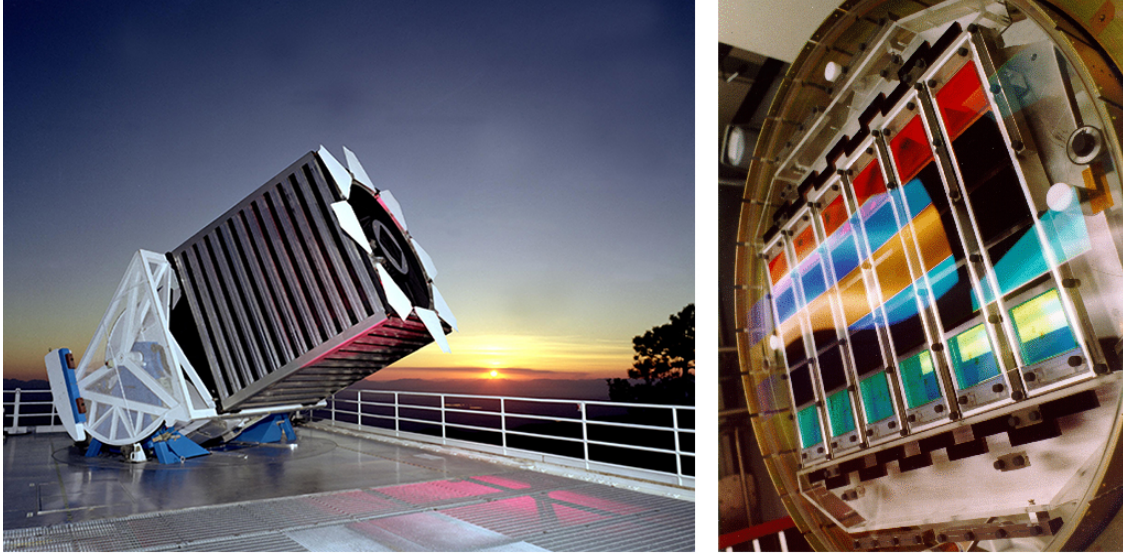


Figure 9: *Left:* SDSS 2.5m telescope at APO.¹ *Right:* SDSS Legacy Survey camera.²

star to track with it. While a star may only be located on a single pixel for less than a second, the final image will have an integrated exposure length of almost a minute.

SDSS imaged the sky using five different filters, *ugriz*, and to do so built one of the most complex cameras in all of astronomy, shown in figure 9. Each column of the camera contains 5 CCD chips, each with a different SDSS filter above it. A star would move across the column of chips (top to bottom in the picture), being imaged through each of the five filters in quick succession. To cover large areas of sky at a time, the camera contained six of these filter columns.

From 2000 to 2008, the SDSS Legacy Survey imaged more than 8200 degrees of sky, covering several of the clusters in this project. Magnitudes released from SDSS were measured using aperture photometry; such a large area of sky required the least computationally costly approach. Most of the region imaged by the Legacy Survey was in the low density halo of the Milky Way, where aperture photometry works accurately.

Magnitudes for stars in the densely packed globular and open clusters in the imaged region were unable to be measured by the aperture photometry technique. An et al. (2009) re-derived magnitudes for several globular and open clusters within the Legacy Survey region using PSF photometry. The open clusters NGC 2682 (M67), NGC 2420 and NGC 6791 were included in this work, with magnitudes down to $g \sim 23$.

MOSAIC: The MOSAIC instrument, outfitted with *UBVRI* filters, contains an array of eight 2048-by-4096 pixel CCD chips to create a single 8192-by-8192 pixel image. While it has been attached previously to the 4-m telescope at Kitt Peak National Observatory (KPNO) in Arizona, the data used in this project is from the WIYN 0.9-m telescope at KPNO. With roughly a square degree field of view, the MOSAIC images will allow us to analyze the entire spatial extent of any cluster observed.

¹<http://astro.uchicago.edu/~frieman/SDSS-telescope-photos/sdss-telescope.jpg>

²<http://www.sdss.org/dr3/instruments/imager/faceplat.gif>

WOCS collaborator Ata Sarajedini obtained images of several open clusters with MOSAIC: NGC 1039 (M34), NGC 1960 (M36), NGC 2099 (M37), NGC 2168 (M35) and NGC 2682 (M67). *UBVRI* photometry for M35 has already been obtained (Sarajedini & Kinemuchi, *private communication*) down to $V \sim 20$. Photometry of the other clusters is currently underway at TCU.

2.3.2 Near-Infrared Data Sources [1.0 – 2.5 μm]

2-Micron All Sky Survey (2MASS): Similar to the goals of SDSS Legacy Survey, 2MASS aimed to observe the entire sky in the near-IR and catalog all detected stars and galaxies. To image the entire sky, 2MASS utilized two different observatories: Mt. Hopkins in Arizona for the northern hemisphere, and Cerro Tololo Inter-American Observatory (CTIO) in Chile for the southern hemisphere. Beginning operations in 1997, 2MASS achieved its goal by 2001; covering over 99% of the sky, and cataloging more than 300 million point sources. The 2MASS data set is *shallow* — it only contains fairly bright stars — with limiting magnitudes in JHK_S of 16, 15, and 14.5, respectively.

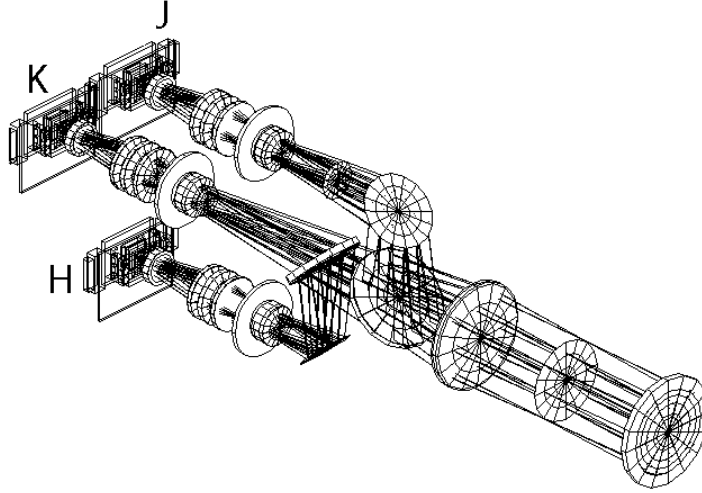


Figure 10: Diagram of 2MASS Camera. Each filter is labelled.

Each 2MASS telescope utilized a custom camera in order to efficiently image the sky using all 3 near-IR filters (JHK_S). Instead of revisiting the same fields three times, the 2MASS instrument observed using all three filters in parallel. Incoming light is split using a dichroic for the J filter. Light below a certain wavelength is reflected to the J filter camera, while the rest of the light is transmitted. Another dichroic, this time for the H filter, splits the remaining light to the H and K_S filters. Each filter is coupled with a HgCdTe IR detector. Using this setup, shown in figure 10, each field can be observed in all filters under the same conditions.

NOAO Extremely Wide Field Infrared Imager (NEWFIRM): NEWFIRM is a 1-2.4 μm IR camera, containing 2MASS JHK_S filters, and located on the Mayall 4-m telescope at KPNO.

NEWFIRM consists of a grid of four 2048-by-2048 InSb detectors to create a 4096-by-4096 image. Dr. Frinchaboy observed the clusters NGC 2099 (M37), NGC 2168 (M37) and NGC 2682 (M67) in early 2008. While NEWFIRM’s field of view is only a quarter of a square degree (half degree on each side), multiple pointings were used to generate a seamless square degree image around each cluster.

The deep images (10 – 40 min exposures) have been reduced at TCU using PSF photometry. Calibrating to 2MASS magnitudes, this yielded magnitudes down to $J \sim 21$. Combined with 2MASS, these clusters have near-IR photometry over a 15 magnitude range, corresponding to a brightness ratio between the brightest and dimmest stars of nearly 1 million. The NEWFIRM photometry will allow study of low-mass systems in these clusters.

Infrared Side Port Imager (ISPI): Dr. Frinchaboy, along with WOCS collaborator Karen Kinemuchi, obtained deep near-IR data of the clusters IC 4651 and Collinder 261 taken with ISPI on the Blanco 4-m telescope at CTIO. ISPI consists of a 2048-by-2048 HgCdTe IR detector with a 10 arcminute field of view. Due to the small field of view, images cover only the core of each cluster. Photometry has been completed (Kinemuchi, *private communication*), yielding magnitudes down to $J \sim 18$.

Near Infrared Imager (NIRI): The Gemini Observatory consists of 8-m telescopes in both hemispheres: Gemini-North on Mauna Kea in Hawaii, and Gemini-South on Cerro Pachón in Chile. J and K_S images of the cluster NGC 6791 were taken using Gemini-North by WOCS collaborator Ted von Hippel over several nights in 2003. These observations utilized Gemini-North’s NIRI instrument; a 1024-by-1024 InSb detector with a field of view of 2 arcminutes. Images were sent to TCU where I analyzed them using PSF photometry. While lacking in spatial coverage, the NIRI images contain faint cluster stars, with a limiting magnitude of $J \sim 21$.

CPAPIR: CPAPIR is a 2048-by-2048 HgCdTe-based IR camera attached to the 1.5-m telescope at CTIO, giving a half degree field of view. Dr. Frinchaboy has obtained J and K_S images of the clusters NGC 3680 and Melotte 66 in February 2007. These images will be reduced and photometered by undergrads either at TCU, or as part of a REU project.

2.3.3 Mid-Infrared Data [2.5 – 10 μm]

Mentioned in 1.1.2, atmospheric absorption beyond 2.5 μm becomes too strong to attempt observations from the ground. The mid-IR data in this project was taken using the *Spitzer* Space Telescope’s Infrared Array Camera (IRAC) (Fazio et al. 2004). For the shorter wavelength IRAC filters, [3.6][4.5], a InSb IR detector is used. For longer wavelengths, InSb detectors do not work (band gap limiting wavelength of 5 μm); the two longer wavelength IRAC filters, [5.8][8.0], are fed to a SiAs detector instead.

IRAC observations were obtained of all 18 clusters by Dr. Frinchaboy. The data were taken in High Dynamic Range (HDR) mode, which captures two images: a 1.2s image and a 30s image. The two images are then combined in order to “fix” saturation of bright stars in the 30s image by using data from the 1.2s image. This approach provides photometry for both bright and faint cluster stars simultaneously.

The photometry was processed utilizing the Galactic Legacy Infrared Mid-Plane Survey Ex-

traordinaire (GLIMPSE) data pipeline (Benjamin et al. 2003), which was modified to handle the HDR data. Average limiting magnitudes in each band are 18, 17, 15 and 14, respectively.

2.3.4 Membership Data

When observing a cluster, not all stars within the frame are *members* of the cluster. Stars that fall along the same line of sight but are in front of or behind the cluster may be confused with cluster stars on a two dimensional image. Our analysis assumes all stars having similar properties, so removing these non-member stars from the sample is beneficial. There are two ways to determine membership, with one way being to use RV measurements. All member stars will have RVs close to the bulk RV of the cluster. Stars in the field will be moving with different speeds, according to their orbital path around the center of the galaxy. Trimming out stars with non-consistent RVs will remove many of the non-member stars in the frame.

A RV gives a star’s velocity along the line of sight to Earth, while *proper motion* gives the star’s velocity in the other two dimensions. A proper motion is measured by taking images of the cluster over a long time baseline — usually years, sometimes decades — and correlating star positions through time. Distant objects, such as galaxies, are assumed to not move over such a time scale, and positions of the stars in each frame are accurately measured in relation to these stationary objects. Computing the change in position of a star as a function of time will yield the proper motion of the star in units of milliarcseconds per year. Only with knowledge of the distance to a star can a proper motion velocity be turned into true velocity (in m/s). Similar to RV member selection, stars with proper motion velocities inconsistent with the bulk motion of the cluster are rejected as non-members.

Having membership data (RV or PM) is key to lightening the load on the fitting codes used in this project. Having membership studies will also provide an important check on our fitting routines if they declare confirmed member stars from previously published studies as non-members.

2.3.5 Data Overview

Table 3 summarizes the available data for use in this project, from the sources listed above as well as from literature. 2MASS near-IR and IRAC mid-IR data are available for all clusters and are therefore not listed in table 3. The clusters bolded in table 3 have complete data sets and were used in this preliminary work. Data sources italicized are ones that are currently being processed and are not currently available for analysis.

3 Testing Stellar Evolution Models

To understand the formation and evolution of the Milky Way and other galaxies, ages of stars must be determined. However, determining the age of a single star is nearly impossible. The Sun is dated not through direct observation, but from radioactive dating of meteorites. Instead of mapping galactic evolution through single stars, star clusters are used, where direct age determination is possible.

Cluster	Visual Data	NIR Data	Membership Data
Berkeley 39			
Collinder 261	Gozzoli et al. (1996)	ISPI	
IC 4651		ISPI	
Melotte 66		<i>CPAPIR</i>	
NGC 188	WOCS Stetson et al. (2004)		RV (Geller et al. 2008) PM (Platais et al. 2003)
NGC 1039 (M34)			
NGC 1817			PM (Balaguer-Núñez et al. 2004)
NGC 1912 (M38)	<i>MOSAIC</i>		
NGC 1960 (M36)	<i>MOSAIC</i>		
NGC 2099 (M37)	<i>MOSAIC</i>	NEWFIRM	
NGC 2158			
NGC 2168 (M35)	MOSAIC	NEWFIRM	
NGC 2420	SDSS		
NGC 2477			
NGC 2682 (M67)	SDSS <i>MOSAIC</i> Yadav et al. (2008)	NEWFIRM	PM (Yadav et al. 2008)
NGC 3680		<i>CPAPIR</i>	
NGC 6791	SDSS	Carney et al. (2005) NIRI	
NGC 6819			RV (Hole et al. 2009)

Table 3: Available data for all clusters in this project.

3.1 Building a Star

To date star clusters, stellar evolution models called *isochrones* are used. Isochrones are sets of synthetic stars with the same chemical composition and age, but with a range of mass, similar to the observed stars in a cluster. Isochrone stellar models are built using two components:

Stellar Core: Using the mass and age of the star, stellar evolution models return two values: the star’s temperature and the star’s surface gravity. The temperature of the stellar core determines where the star falls horizontally on the CMD, while the surface gravity determines where the star is located vertically. Dwarf stars (stars on the main sequence) are small and compact (like the Sun), while giant stars are large and puffy. Even though a giant and dwarf may have the same temperature, the surface gravity of the dwarf will be much higher. Using Newtonian gravity ($g = GM/R^2$), the radius of the star can also be modeled.

Stellar Atmosphere: On first approximation, the energy output of a star is a near-blackbody, governed by the temperature derived for the core model. In reality, the spectrum also has absorption lines from elements in the star’s atmosphere. Temperature and surface gravity from the core model are combined with individual elemental abundances determined for the star and fed into atmosphere generation codes. These atmosphere codes, such as ATLAS9 (Castelli & Kurucz 2004), use this information to compute the strength of all atomic and molecular absorption lines. These lines are overlaid on the blackbody spectrum and the synthetic flux is output.

To convert to magnitudes, the flux curve is convolved with a filter transmission function (those plotted in figure 1) to determine the overall amount of flux coming through the filter. Equations (3) or (4) is then used to convert the flux to a magnitude, depending on which convention you are using.

There are several different isochrone systems, each using different parameters and equations. Differences between systems include:

1. **Equation of State:** The equation of state for a star describes the interaction of gravity and photon pressure within a star. The equation of state for different isochrone systems are not always the same, leading to different estimates for the size and temperature of the star.
2. **Mixing Length:** The mixing length governs how far a single cell can move during convection before being disrupted. During the RGB phase, a star’s outer layers are convective, and the mixing length governs how far materials can move within the star. Larger mixing lengths can allow for fusion products to rise to the surface, altering the chemical composition of the stellar atmosphere.
3. **Core Overshoot:** As Hydrogen fusion slows in the stellar core, the convective zone in the core may increase slightly. This convective zone causes Hydrogen above the core to be pulled in, providing extra fuel for fusion. This addition of fuel causes an abrupt increase in energy output as the star becomes brighter and hotter. This manifests as a blue-ward “hook” in the model CMD, illustrated in figure 11. The amount of convective expansion, and for what mass stars this happens, differs between systems.
4. **Helium Fraction:** The fraction of Helium within a star is not the same between isochrone models. Both the baseline amount of Helium (for a star with no metals), as well as the Helium-to-metal ratio changes between systems.

The physics of stellar evolution and the inner workings of a star are still not completely understood. By comparing multiple isochrone systems to observational data, we will attempt to determine which evolution model contains the most accurate physics. [Question 1]

3.2 Infrared Calibration

Isochrone systems are most often calibrated using visual magnitudes, and have yet to be extensively tested and calibrated in the infrared. Using isochrones in the infrared is important, mainly due to the fact that light can penetrate galactic dust much better using those bands. For a star with 1 magnitude of extinction in H (middle of near-IR), it has 6 magnitudes of extinction in V (middle of visual), using table 2. Compensating for this 5 magnitude difference corresponds to a 10x increase in telescope size; the difference between a modest 1-m class telescope and one of the 10-m Keck telescopes, the best in the world.

Because smaller telescopes can probe further using infrared bands, many new open clusters are being discovered in the infrared only. In order to characterize these new clusters, isochrones must be trustworthy when using only near-IR filters. Currently, the best fit parameters of a particular cluster will change based on what magnitude-color combination is used. Even though the same stars are used, the derived parameters change when using V vs $B - V$ or K_S vs $J - K_S$, etc. Until the discrepancy between magnitude-color combinations is resolved, cluster parameters for NIR-only open clusters cannot be satisfactorily determined.

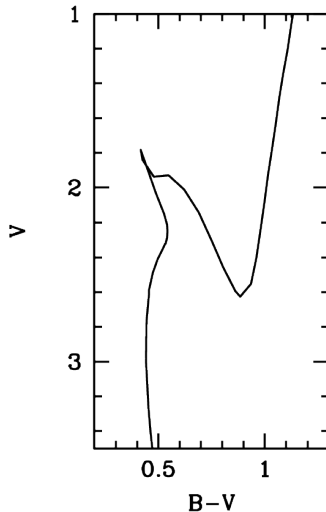


Figure 11: Upper main sequence, turn-off and lower RGB region of 2 Gyr isochrone. Core overshoot hook noticeable at beginning of turn-off.

3.3 Isochrone Fitting

Stars in an isochrone set trace a line on a CMD called the *fiducial ridgeline*. Determining the four cluster parameters (age, distance, metallicity, reddening) amounts to fitting the CMD of the cluster in question to the most accurate fiducial ridgeline.

Age and metallicity affect the shape of the ridgeline, with age moving the turnoff point further down in magnitude while metallicity affects the slope of the RGB on the CMD. Distance simply shifts the fiducial ridgeline vertically in accordance with equation (8). Gas clouds between Earth and the cluster in question contribute two effects: it shifts the ridgeline vertically an amount A_X due to extinction in a particular filter X , as well as shifts the ridgeline horizontally an amount $E(X - Y)$ due to reddening in the $X - Y$ color. The ratio $R_X = A_X/E(X - Y)$ is known for a number of filter systems, and so the ridgeline is shifted along a line with slope R_X on the CMD. The effects of various parameters on the ridgelines is illustrated in figure 12.

In the past, cluster parameters were derived using hand-fit isochrones. With multiple clusters to fit, as well as hundreds of color-magnitude combinations, make hand fitting isochrones ill-advised. With the advent of powerful computers, isochrone fitting can be accomplished much faster digitally. The isochrone fitting routine (Irwin, *private communication*) used in this research, called IsoFit, creates a grid of ridgelines with all possible combinations of age, distance, reddening and metallicity to compare to the observational data. The effects each parameter has on the ridgeline is described below. Ridgelines with varying parameters are shown in figure 12.

1. **Metallicity:** Metallicity governs the strength and abundance of absorption lines present in the stellar atmosphere. As metallicity increases, so do line strengths, removing more photons from the spectrum of the star and changing both the magnitude and color of the star. Underlying physics, such as core overshoot, depends on metallicity in some models as

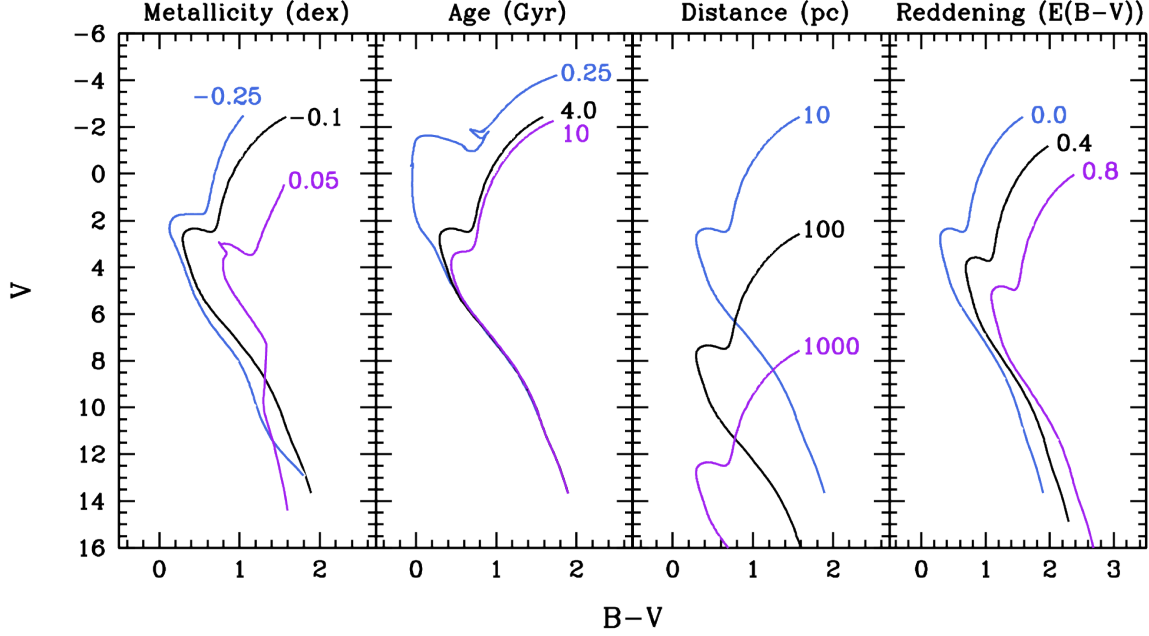


Figure 12: Effects of parameters on ridgeline. Default ridgeline values are: $Z = -0.1$ dex, Age = 4 Gyr, Distance = 10 pc, Reddening = 0. For each panel, only the relevant parameter is changed while the other three are held at the default value.

well.

2. **Age:** Age governs the location of the turn-off on the CMD. As time progresses, lower mass stars, and hence dimmer, expend their Hydrogen fuel and enter the subgiant branch. Core overshoot models are often limited for stars above a certain mass, and once those stars have evolved to the RGB, the overshoot hook no longer exists in the ridgeline.
3. **Distance:** Distance alters the location of the ridgeline on the CMD according to equation (8), due to the inverse-square law of light intensity. Ridgelines with larger distances will be shifted down in magnitude.
4. **Reddening:** On a CMD with magnitude X and color $X - Y$, reddening shifts the ridgeline along a line with slope $R_X = A_X/E(X - Y)$. R_X can be computed using values in table 2 for all of the CMDs used in isochrone fittings. Reddening is always positive, shifting the ridgeline to the left and down on the CMD.

Each ridgeline is placed on the CMD and each data point compared to it. For each point, the closest distance from the point to the ridgeline, D , is computed. The fit value for the ridgeline is calculated using:

$$\text{Fit} = \sum_{\text{stars}} \left[D_i + \sqrt{(\sigma_X)_i^2 + (\sigma_{X-Y})_i^2} \right] \quad (24)$$

In equation (24), σ_X and σ_{X-Y} are the photometric errors in magnitude and color, respectively. Due to observational uncertainties, the “closest” a point can be to the ridgeline is equal to its errors. If a ridgeline fits well, all D_i ’s will be low, and the total Fit value will also be low. After all possible ridgelines have been compared, the one with the lowest Fit value is chosen as best. The parameters of this best-fit ridgeline are taken to be the parameters of the cluster itself. To determine the errors in parameter determination, the standard deviation of the D_i ’s is converted into a parameter error.

Observational data of clusters over many photometric bands will be run through the fitter and compared with published ages, metallicities, distances and reddening values. The isochrone systems that show consistent and accurate parameter determination will be marked as best, signifying the most realistic physical model.

3.4 APOGEE

Of the four cluster parameters used by IsoFit, metallicity is the hardest to determine photometrically. To simplify the fittings, we will utilize metallicity information from the APO Galactic Evolution Experiment (APOGEE). As a part of SDSS-3, APOGEE will use high-resolution ($R \sim 22500$), high signal-to-noise (100/pixel) infrared spectroscopy to determine precise radial velocities and chemical information for 100,000 red giant stars. Many of the clusters in this project will be observed by APOGEE, and we will restrict the IsoFit grid to isochrone models with a single metallicity as determined by APOGEE measurements.

3.5 Preliminary Results

Preliminary results for this technique were obtained using the cluster M67. With deep visual, near-IR and mid-IR photometry, a published RV study and published metallicities, M67 makes an ideal candidate to test isochrones over a wide range of filters. All possible magnitude-color combinations were fed into IsoFit, and output parameters collected. Each fit parameter is converted into a gaussian parameter distribution with σ equal to the errors from the fit, and then added together to compute the overall distribution. Heights are scaled by the minimum grid spacing ($\Delta \log(\text{Age}) = 0.05$, $\Delta(m - M) = 0.05$, $\Delta E(B - V) = 0.01$) to bring all parameters to a common scale.

3.5.1 Comparison

Using the M67 dataset, we have analyzed isochrone fits using two different tests.

1. **Padova vs Dartmouth:** Of the many isochrone systems available, the Padova system (Girardi et al. 2002) is by far the most widely used due to its ease of use and the multitude of filter magnitudes available. We will use our isochrone fit results to compare the performance of the Padova system to others, such as the Dartmouth system (Dotter et al. 2007) in order to determine which most accurately models a wide variety of clusters.
2. **Visual vs Near-IR:** By comparing isochrone fits in visual and near-IR only CMDs, we will address the issues of isochrones in infrared bands, discussed in 3.2. We will determine whether certain isochrone systems determine consistent parameters in both regions, or whether there are systematic offsets when using near-IR bands, compared to visual.

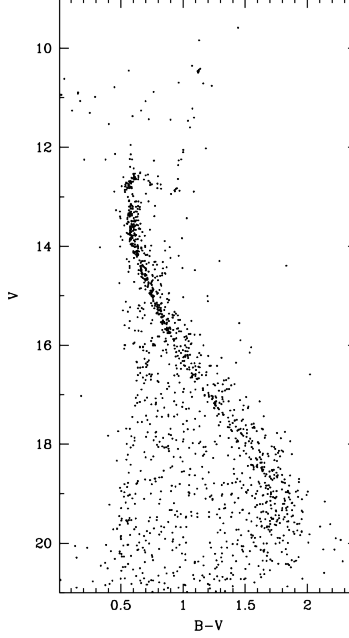


Figure 13: Full M67 data set CMD.

3.5.2 Full Cluster Set

A CMD of the M67 data set is shown in figure 13. While the main sequence and RGB are clearly visible, there are many field stars included as well. These field stars will negatively impact the fitting, adding large numbers to the fit in equation (24). The errors in the fits, which are computed based on the scatter in distances, will also be negatively impacted by the inclusion of non-member stars in the IsoFit dataset.

3.5.3 Membership Cut

In order to improve the isochrone fits and cut down on the scatter in parameters, we limited our next sample only to confirmed cluster members. Using a WOCS RV study of M67 (Mathieu et al. 1997), we select only confirmed single member stars within the cluster. The full data set is compared to the single member set in figure 14. The RV-trimmed set does not have any stars below $V \sim 16.5$, so it will not be able to test the low mass stars in the isochrone models, but it will test parameter determination for a very clean stellar sample.

IsoFit was run using a single metallicity of $Z = 0.019$, while the other three parameters were given their full range. Age ranged from 4 Myr to 14 Gyr for Padova and 250 Myr to 14 Gyr for Dartmouth. Distance ranged from 160 pc to 6.3 kpc. Reddening ranged from 0.0 to 1.5.

A comparison of IsoFit results for both isochrone systems is shown in figure 15. Both systems show close agreement in distance and age, at 3.3 Gyr and 845 pc. These values are very close to the published values of Grocholski & Sarajedini (2003). Dartmouth’s primary reddening peak at $E(B - V) = 0.05$ is close to the published value, with a smaller peak at higher reddening. Padova most often chooses a reddening of $E(B - V) = 0.0$, with a smaller peak at the location of Dartmouth’s primary. Overall, IsoFit does a good job of picking out reasonable parameter values

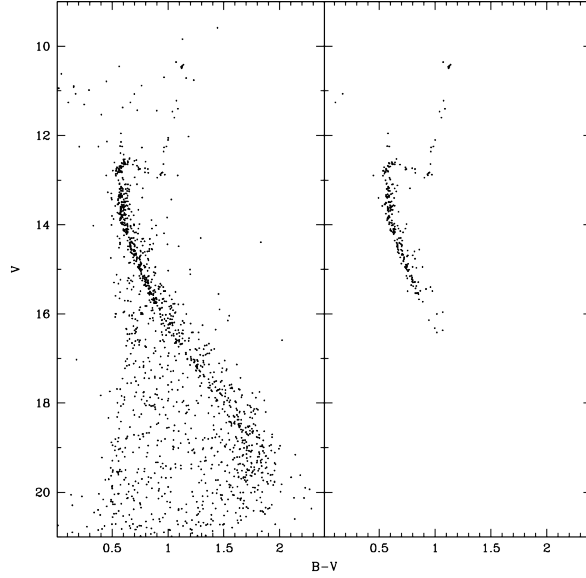


Figure 14: V vs $B - V$ CMDs for full M67 dataset (left) and only RV-confirmed single member stars (right).

from a large parameter space with the RV-cleaned sample.

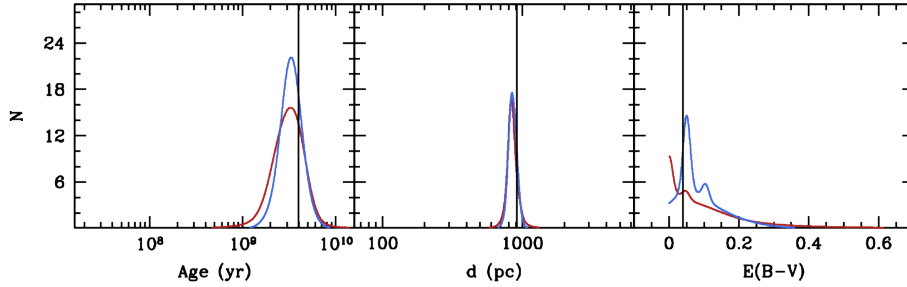


Figure 15: Comparison of IsoFit results for the RV-cleaned M67 dataset. Values for Padova system in red, Dartmouth in blue. Black vertical lines are literature values from Grocholski & Sarajedini (2003).

Figure 16 shows results from both systems when using visual or near-IR CMDs only. Besides Padova reddening determination for near-IR CMDs, which shows no clear peak, parameters determined for visual CMDs track closely with those from the near-IR.

3.5.4 Empirical Ridgeline

Selecting only RV members clean the sample considerably, but at the cost of losing all low-mass stars. To trim the set of all background contamination while still keeping the low-mass members, we apply an *empirical ridgeline*: a hand-drawn main sequence, subgiant branch and RGB. Two

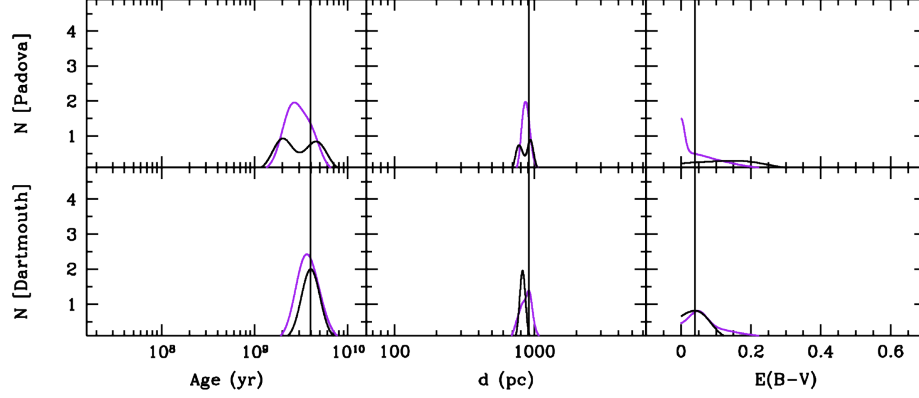


Figure 16: Comparison of IsoFit results for the RV-cleaned M67 dataset. Values for visual only CMD fits in purple, near-IR only CMDs in black. Black vertical lines are literature values from Grocholski & Sarajedini (2003).

empirical ridgelines were applied to the M67 dataset, one in V vs $B - V$, the other in J vs $J - K_S$. The points making up each ridgeline are listed in table 4.

Table 4: Points tracing the empirical ridgelines for M67.

V	$B - V$	J	$J - K_S$
10.712	1.163	6.494	0.83
12.4	0.96	9.045	0.64
12.9	0.9	10.579	0.56
12.577	0.641	10.89	0.5
12.819	0.553	10.998	0.41
13.2	0.58	11.281	0.32
13.724	0.574	12.273	0.32
14.5	0.68	13.168	0.4
15.155	0.775	13.682	0.57
15.672	0.88	14.182	0.71
16.669	1.1	14.933	0.75
17.735	1.395	15.69	0.73
18.122	1.55		
18.813	1.645		
19.7	1.7		

To clean the set, stars are grouped into 0.5 magnitude-width bins and errors in magnitude and color for each star in the bin are averaged together. Then, each data point's distance to the ridgeline is computed. If the distance is more than 3x the uncertainty in the average errors ($\sqrt{\sigma_X^2 + \sigma_{X-Y}^2}$), it is removed. Additionally, if a point does not have a B , V , J or K_S magnitude value, it is removed. The empirical ridgeline is compared to the full and RV-trimmed datasets in figure 17. The empirical ridgeline follows the RV-trimmed set closely above $V \sim 16.5$, including many confirmed singles into the ridgeline-trimmed dataset, while accurately trimming the CMD

down to $V \sim 19$.

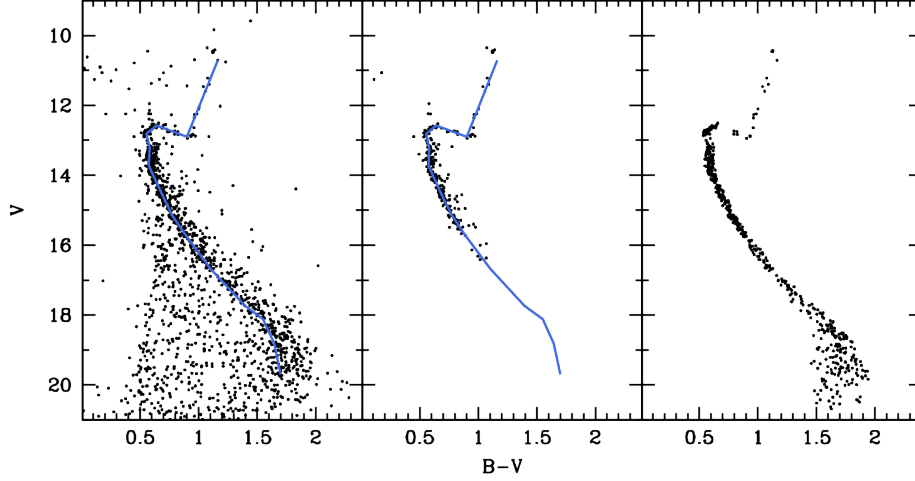


Figure 17: Empirical ridgeline in V vs $B - V$ overlayed on the full data set (left) and RV-cleaned set (middle). Empirical ridgeline-cleaned CMD (right).

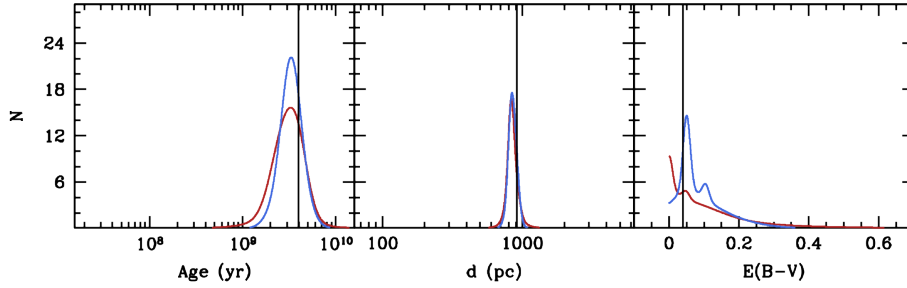


Figure 18: Comparison of IsoFit results for the ridgeline-cleaned M67 dataset. Values for Padova system in red, Dartmouth in blue. Black vertical lines are literature values from Grocholski & Sarajedini (2003).

This set is fed into IsoFit with the same full-parameter grid used in the previous RV-trimmed case. Parameter distribution results for both isochrone systems are shown in figure 18. The results from the ridgeline-trimmed set are almost identical to those from the RV-cleaned sample, with a slight change in reddening distributions. The turn-off, which is included in both data sets, is one of the most important features for age and distance determinations, leading to the similar distributions. The ridgeline-cleaned set has less scatter in color, which may have led to the shift in reddening output.

In figure 19, the ridgeline-cleaned CMDs are compared to the best fit isochrones in V vs $B - V$, V vs $V - K_S$ and J vs $J - K_S$. We compare the fits of these isochrones in two areas:

1. **Turn-Off:** In the data, there is a distinct blue hook around the turn-off. The Padova isochrone replicates this feature accurately, while the Dartmouth isochrone has a much less

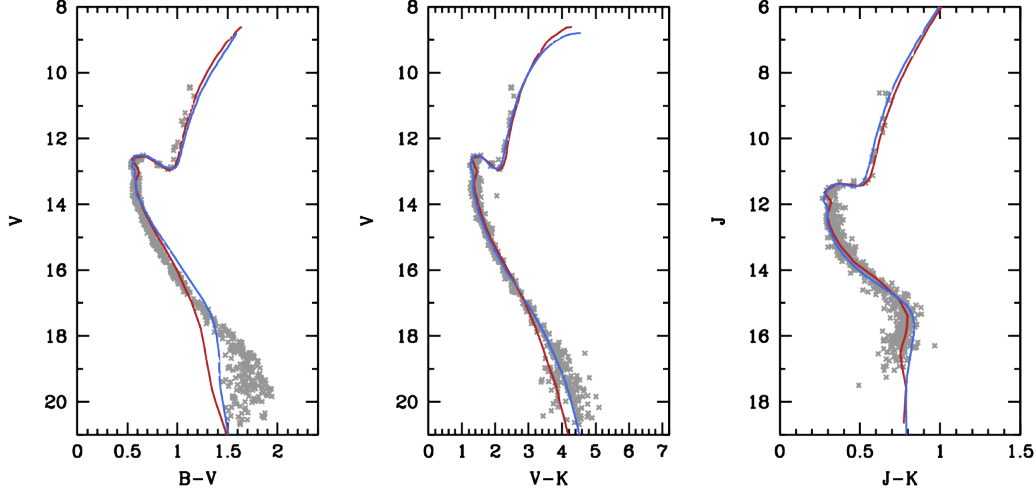


Figure 19: Best-fit isochrones to empirical ridgeline-cleaned data. Isochrones have $E(B - V) = 0.0$, $d = 800$ pc, age = 4 Gyr. Dartmouth isochrones in blue, Padova in red.

pronounced hook. For the 4 Gyr isochrone, the Padova model predicts the correct amount of core overshoot.

2. **Lower Main Sequence:** Both isochrone systems accurately follow the near-IR MS more closely than in the visual. Problems with the models of low-mass stars cause their temperature to be over-predicted in visual bands, and slightly under-predicted in near-IR bands. A mix of the two systems cancel these effects out, and cause the isochrones to track closely to the observed data. The Dartmouth model in $V - K_S$ fits observation down to the limiting magnitude of $V \sim 21$.

These effects can be attributed to many different parts of the models. The Dartmouth model switches to an alternate equation of state for stars less than $0.7 M_{\odot}$, corresponding to a magnitude of $V = 17.5$ in M67. This is approximately the location of an abrupt downward turn in the visual. Alternately, there could be a problem with atmosphere models of low-mass stars, causing incorrect absorption lines to be placed into the synthetic spectrum. By testing other clusters and other isochrone systems, we will better understand what physics cause these problems at low mass.

3.6 Future Work

Continuation of this project will focus on three distinct improvement areas.

3.6.1 Additional Systems

Padova and Dartmouth isochrone systems are the most widely used, but they are far from the only two. Other known isochrone systems, including the Yale-Yonsei (Demarque et al. 2004), Victoria-Regina (VandenBerg et al. 2012; 2006), and YREC (An et al. 2006) models will be added into the isochrone fitter and run on the same clusters to compare results.

The reason that Padova has become ubiquitous and Dartmouth has become second is due to the wide number of filter systems included in the isochrone files. IRAC filter magnitudes are only found in the isochrone models of Padova and Dartmouth. These filters may have to be neglected in fits to other isochrone systems, or a mechanism for creating these filter magnitudes from the models will have to be created.

3.6.2 Separating the Models

Isochrone systems consist of two parts: A core and an atmosphere. When comparing two isochrone models, an improvement in the fitting can be attributed to either the core model being better, the atmosphere model being better, or both. As of now, there are too many free parameters to deduce the accurate physics from these fits. To counter-act this, we hope to split the isochrone models into component pieces and analyze the cores separate from the atmospheres.

To do this, the atmosphere models used must be standardized. The resulting fits will only be testing the stellar core models. ATLAS9 can generate atmospheres for stars of any temperature and surface gravity. Using these atmospheres, we can extract filter magnitudes and create our own isochrone sets. The best models using this set will be attributable solely to the core model; those that perform best will be noted as having the most accurate core physics. After all core models have been tested, different atmosphere models can be used as well, such as ATLAS12 or OPAL (Iglesias & Rogers 1996). Best fits here will be attributable only to improved atmosphere physics. By breaking the problem into two sets, underlying physics can be deduced more easily.

3.6.3 Binaries

Some of the spread in isochrone fits can be attributed to binary stars within the clusters themselves. Isochrone ridgelines are theoretical *single* star sequences, and fits of mixed populations will result in scattered results. Using the techniques discussed in 4, we will clean binaries from these data sets, and re-attempt the fittings.

4 Binary Cluster Populations and Evolution

4.1 Effects of Binary Stars

4.1.1 Effect on Stellar Evolution

Binary systems are known to have effects on stellar evolution, allowing the creation of non-standard stars, such as *blue stragglers*. When a star consumes all of its Hydrogen fuel in the core, it begins to expand and moves onto the sub-giant branch on a CMD. In many clusters, however, large stars are observed on the main sequence above the turnoff, meaning that they have continued burning hydrogen in their cores longer than expected. These stars are termed blue stragglers, as they linger on the hotter main sequence instead of following the cooler sub-giant branch.

Many blue stragglers have been confirmed to be part of a cluster through RV measurements, so it is unlikely they are contamination from field stars. The leading theory of blue straggler formation hypothesizes that blue stragglers are main sequence stars that were at some point a member of a binary system with a larger star (Geller & Mathieu 2011). As the larger star evolves off of the main sequence and increases in size, the pre-blue straggler begins to siphon off mass from its companion.

The influx of mass allows the pre-blue straggler to access more Hydrogen than it normally would, and continue burning on the main sequence for longer than conventional models predict.

If this theory is correct, we should find a correlation between the percentage of binaries and frequency of blue stragglers. Using our large cluster set, we will test this theory of blue straggler evolution more rigorously than ever before. **[Question 3]**

4.1.2 Effect on Cluster Evolution

Open clusters are not infinitely-lived; they slowly “evaporate” away and disappear over a few Gyr on average. The destruction of open clusters is predominantly a result of two effects:

Cluster Heating: Stars within the cluster can transfer energy to one another through gravitational interactions. When a small star passes by a large one, it may pick up energy from the interaction, which may accelerate the smaller star past the escape velocity of the cluster. These internal interactions will “boil off” many of the smaller members of the cluster, starting the cluster destruction process.

Tidal Friction: The *tidal radius* of an open cluster is the radius within which all the stars are gravitationally bound; stars outside of the tidal radius are no longer gravitationally bound and are lost to the cluster. When a cluster is far from all other large gravitational sources, the tidal radius of the cluster stays fairly constant, r_{t0} . However, when the cluster passes by a large mass, such as a spiral arm or giant molecular cloud, the tidal radius shrinks to r_t as the outside mass pulls on the outer members of the cluster. Cluster stars that are now outside of r_t move away from the cluster under the influence of the foreign mass.

After the cluster passes the large mass, the tidal radius expands back to its original size, but some of the cluster stars have moved enough such that they are now outside of r_{t0} and are therefore no longer bound to the cluster. Large clumps of mass are common within the galactic disk, and multiple of these “collisions” will remove many of the cluster members over a few Gyr.

Binary systems within a cluster add to cluster heating by contributing not only their orbital energy during an interaction but also the internal energy of the system. To understand what effect this has on interactions, the orbital energy of the system is compared to the internal energy of the system itself. A theoretical cluster is assumed to have a mass of $1000 M_\odot$, while the theoretical binary system orbits at a radius of 5 ly from the cluster center. The binary system has a primary star mass of $2 M_\odot$ and an average separation of 20 AU.

$$E_{cluster} = \frac{GM}{R} = \frac{(6.67 \times 10^{-11})(1000(2 \times 10^{30}))}{5(9.46 \times 10^{15})} = 2.82 \times 10^6 \text{ J} \quad (25)$$

$$E_{internal} = \frac{GM}{R} = \frac{(6.67 \times 10^{-11})(2(2 \times 10^{30}))}{20(1.49 \times 10^{11})} = 8.95 \times 10^7 \text{ J} \quad (26)$$

There is more than an order of magnitude more energy locked within the orbit of the binary system than in the rotation around the cluster center. The massive increase in interaction energy with binary systems will lead to quicker “boiling off” of clusters with a high percentage of binaries. We will accurately determine the percentage of binaries within a cluster and correlate it with cluster destruction timescales.

4.2 Current Binary Detection Techniques

4.2.1 Two-Band Photometry

Binary stars will be brighter than a single star with the same mass as the primary, due to additional flux from the secondary star. In addition, the star's color will be shifted by the smaller (and hence redder) star. When plotted on a CMD, main sequence binary stars will be offset above and to the right from the single star main sequence. Considering the special case of an equal-mass binary system, the binary system will have the same color as a component single star, but will be twice as bright. Using equation (2), we find the difference in magnitudes:

$$m_S - m_B = -2.5 \log_{10} \left(\frac{F_S}{F_B} \right) = -2.5 \log_{10} \left(\frac{F_S}{2F_S} \right) = 0.753 \quad (27)$$

An equal-mass binary system will be located 0.753 magnitudes above the corresponding single star on a CMD. Binaries with a mass ratio less than one will be located at various locations between the single star main sequence and the equal mass binary sequence on the CMD. Two-band photometry studies attempt to measure the binary properties of a cluster using a single CMD by measuring the distance between a star and the single star main sequence.

The distance a binary star is from the single star main sequence depends not only on the mass ratio of both stars, but also the primary mass. Figure 20 shows the position of binary stars on a CMD for various primary masses and mass ratios. Binaries with a mass ratio of 0.5 (open squares) lie close to the single star main sequence for primary stars with mass $< 2M_\odot$ and close to the equal mass binary sequence for primary masses of $> 3M_\odot$.

This binary detection technique is very sensitive to errors. For low mass primaries, small color errors will blend together single stars and binaries with a mass ratio of 0.5 because they lie so close together on the CMD. On the high mass end, it becomes hard to differentiate between primary masses, as all binaries with mass ratios greater than 0.5 lie along the equal mass binary track. Figure 20 shows binary positions for high primary masses in a grid of $1 M_\odot$. Attempting to measure using a finer grid is impossible as many binaries will begin to overlap.

Two-band photometry studies are most useful for quickly determining the binary fraction of a cluster. While it is unable to determine individual masses of binary systems, binaries with mass ratios greater than 0.5 can often be grouped together and measured (see Milone et al. (2011)). We are interested in determining the individual mechanics of the binary systems in a cluster, and require a more robust approach.

4.2.2 Radial Velocity Studies

The most accurate way of detecting binaries is through the use of radial velocities (RVs) of spectroscopic binaries (described in 1.2.3). The value of these studies is that individual star orbits can be determined for double-lined spectroscopic binaries and can be inferred from single-lined binaries. A knowledge of the orbits is important to understanding the mechanics of the binary system.

RV studies of cluster binaries, while powerful due to the amount of information they give, are limited in several ways.

Limited Sample Size: Since RVs are determined spectroscopically, there are only a small number of stars that can be measured at a single time. Photometry of a cluster can determine magnitudes

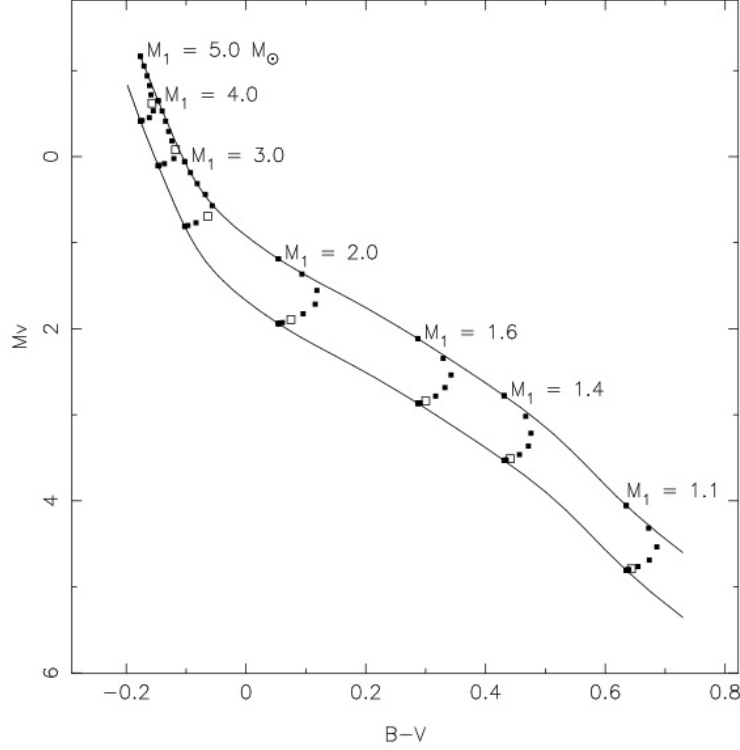


Figure 20: Figure reproduced from Hurley & Tout (1998). Theoretical single star and equal mass binary main sequences for a star cluster covering a range of magnitudes. For each primary mass, points are plotted on the CMD for every binary mass fraction in steps of 0.1. Open squares are binaries with a mass ratio of 0.5.

for thousands of stars with a single image, while spectroscopy, at maximum, can measure spectra for a few hundred stars at once. In order to survey a cluster, a large amount of telescope time must be used to cover all stars.

Multiple Visits: Stellar spectra must be obtained multiple times in order to determine whether a star is a binary or not. Fully characterizing the orbits of both stars requires many repeat observations, depending on the orbital period of the system. This multiplies the necessary telescope time for a quality RV study in order to detect binaries.

Limiting Magnitude: In order to accurately determine a star’s velocity, a certain level of signal-to-noise must be achieved. For a high-resolution spectrometer ($R \sim 20,000$), the incoming flux is spread across all resolution elements. Comparing to a comparable length photometric exposure, we find the limiting magnitude difference:

$$m_{\text{phot}} - m_{\text{spec}} = -2.5 \log_{10} \left(\frac{1}{20000} \right) = 10.8 \quad (28)$$

In the time it will take a spectroscopic measurement to complete on a 10th magnitude star, all stars down to 20th magnitude could be measured photometrically.

Inclination & Orbital Period: Mass determination using double-lined binaries is complicated by the inclination of the system. While RV studies can determine the orbital mechanics of the system, they cannot accurately determine masses. In addition, RV studies are limited by the resolution of their spectrometer; systems with doppler shifts less than the resolution of the spectrometer will not be registered as variable. Only binary systems with short enough orbital periods will produce large enough doppler shifts to be detected.

Both of the current binary detection techniques are inadequate for understanding the mechanics of binary systems in a cluster. We present an alternate method that is able to determine binary parameters for individual systems within a reasonable amount of telescope time.

4.3 Binary SED Fitting

Using multi-filter photometry, we rebuild the spectral-energy distribution (SED) of a star and compare it to those from isochrones. Binary systems will differ from single stars due to excess flux in the red to infrared from the smaller companion. Using isochrone sets, a grid of binary and single stars are built for a specific metallicity, age, distance and reddening. Single star isochrone magnitudes are converted to fluxes using,

$$\hat{F} = 10^{m/-2.5} \quad (29)$$

For a binary with primary star P and secondary star S, the total flux for a specific filter is simply a sum of both constituent stars:

$$\hat{F}_B = \hat{F}_P + \hat{F}_S \quad (30)$$

Combining the two above equations and converting back to a magnitude for the binary star, we find:

$$m_B = -2.5 \log_{10} \left(10^{m_P/-2.5} + 10^{m_S/-2.5} \right) \quad (31)$$

Magnitudes are computed for every possible combination of primary and secondary star mass in all filters. New isochrone files which contain magnitudes for all single and binary stars for a given set of cluster parameters is output and used by the fitting code. In the conversion to flux from magnitude there is a zero point correction that we are neglecting. This zero point cancels in equation (31), so it makes no difference to the result and improves computational accuracy to neglect it.

In order to get accurate results, a star must have at least 9 valid magnitudes. Stars with less than 9 valid magnitudes are skipped during the reduction and no information can be gained. Cluster stars with 9 or more magnitudes are then individually compared to these binary isochrone grids, and assigned a χ^2 value using:

$$\chi^2 = \sum_{\text{filters}} \frac{1}{|m_{\text{observed}} - m_{\text{isochrone}}| + 0.01} \quad (32)$$

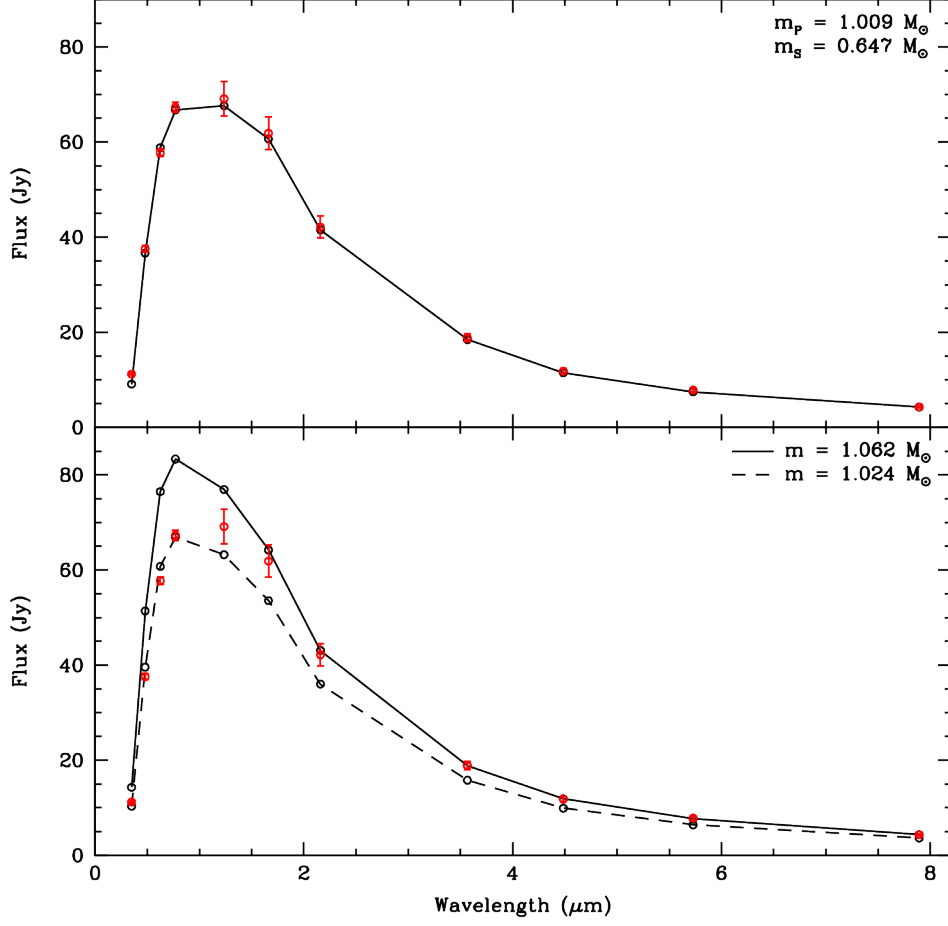


Figure 21: Comparison of star in M67 with model SEDs. (*Top*) Observed fluxes (red) compared to best-fit binary model. (*Bottom*) Observed fluxes (red) compared to two best-fit single star models.

A softening parameter, 0.01, is used to avoid mathematical singularities. To remove magnitudes with large errors, any filters with a fit value of less than 10 is rejected. After the star has been compared to all grid points, the highest χ^2 value is chosen as the best fit and those parameters (primary and secondary masses) are recorded. For a match to be considered, it has to have at least 9 “good” magnitude matches. If no fits have 9 good matches, but the star started with 9 or more valid magnitudes, then the star is classified as a non-member of the cluster.

To account for the errors in the photometry, the grid searching process is Monte Carloed. At the beginning of each iteration, every filter magnitude is sampled from a gaussian error distribution. The best fits from each iteration are recorded, and the fitting program outputs the mean and standard deviation of the best fit results. For the preliminary results, 10 iterations were used, but it is possible to use any number of resamples.

Figure 21 shows the result of a binary fitting on a star from the cluster M67, using 11 of the

12 possible filters: $ugriJHK_S[3.6][4.5][5.8][8.0]$. In the bottom panel, the observed fluxes (red) are compared to the two best-fit single star models. One single star model is chosen to fit the visual data the best, while the other is chosen to fit the mid-IR tail; neither fit the data closely. The top panel shows an improved fit when matching to a binary model. This star was flagged by a previous WOCS RV study as a single, but our technique demonstrates it is fit better as a binary system. The reason for this is discussed in section 4.4.3

4.4 Code Testing

Several tests were performed to measure the fitting routine’s sensitivity to errors. Synthetic photometry from the isochrone files is first re-sampled using gaussian distributed errors, to simulate actual observational data, and then input into the fitter. For the first run, solar-metallicity, 4 Gyr isochrones are used.

4.4.1 Single Star Test

All of the single stars in the isochrone set were input into the isochrone fitter, to test error sensitivity in false positive binary detection. Photometric errors of 0.07, higher than most of the observational data compiled, were used in each filter.

Results of the single star test are in figure 22. Black dots on the figure are stars that were confirmed as single in the fitter, while red stars are those flagged as a binary by the fitting routine. Two problem areas arise: one where the equal-mass binary sequence passes over the subgiant branch, and another where the binary subgiant branch approaches the lower RGB. This test indicates that results for stars near and above the turnoff cannot be trusted, while stars on the main sequence will have few (if any) false positive detections.

4.4.2 Mass Determination Test

A second test was used to determine the accuracy of mass determinations from the fitting routine. For this test, 2000 binary stars were randomly chosen from the entire isochrone grid, and sampled with errors of 0.04 in all bands. This 2000 star set was then run through the fitter and the output masses are compared to the originals. The results are summarized in figure 23.

Similar to the single star test, photometric errors begin to complicate fits above the turn-off (around $1.0 M_{\odot}$). For lower mass stars, primary mass determination is accurate to around 5%, while secondary mass determination is good to roughly 10%.

4.4.3 Real World Test

For the cluster M67, we compare the results from the binary fitting to published RV results in order to check the validity of our fits. The results of this run are shown in figure 24. Noting the problem with binary determination at or above the turnoff, we restrict our results to stars below $g \sim 14$. Stars confirmed as singles or binaries using both methods are colored dark and bright green, respectively.

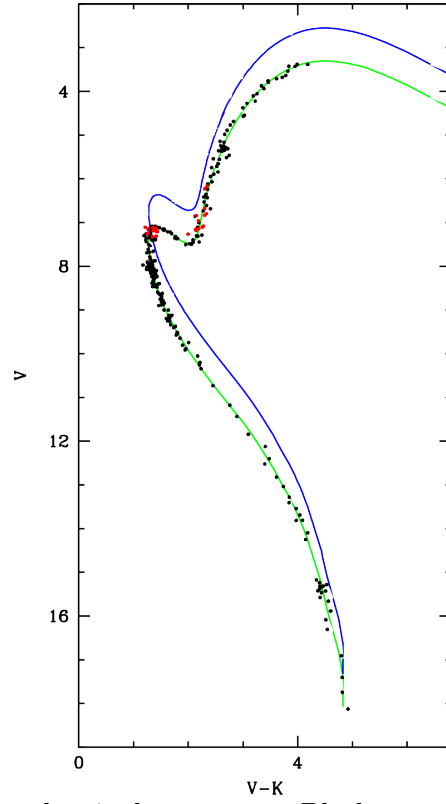


Figure 22: Results for the single star test. Black stars are confirmed singles, red are stars flagged as binaries by the fitting routine. Green line is original ridgeline stars are sampled from, blue is ridgeline of equal mass binaries.

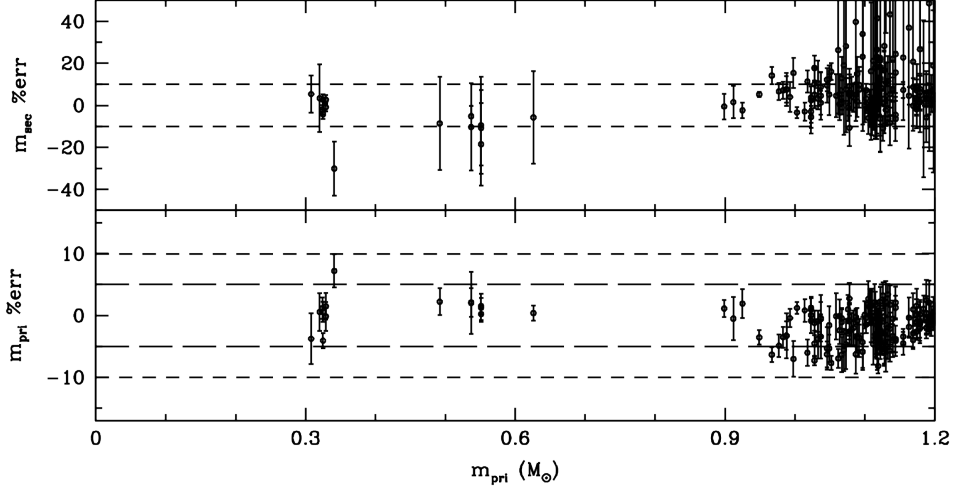


Figure 23: Results for the mass determination test. (*Top*) Percentage error in secondary star mass determination vs primary star mass. (*Bottom*) Percentage error in primary star mass determination vs primary star mass.

Stars colored blue in figure 24 are stars that are measured as singles in the RV study, but our routine marks as binaries. These stars may be pole-on binaries, binary systems with an inclination of 0° , which will show no RV variability but will appear as binaries photometrically. Alternately, systems with long orbital periods may not produce appreciable RV shifts but will show excess flux. The individual fitting of a blue dot star is shown in figure 21.

Stars marked red in figure 24 are RV-measured binaries, but are fit best by single stars in our method. These systems may be ones with very small secondaries, where the flux addition may not be appreciable. RV studies are much more sensitive to these types of systems, and will detect them whereas we will not.

4.5 Future Work

Future work on this project will focus on the following areas:

1. **More Testing:** While the first tests of the binary fitter showed promise, many more testing scenarios are required. Each of the tests used a single age and metallicity, and re-running all the above tests using different values for age and metallicity will further illuminate the fitter's abilities. The young cluster M35 also has a published WOCS RV study and will make a good second test to real-world data.

The exact parameters of a cluster are not always known; a future test will measure the fitter's sensitivity to the four isochrone parameters.

2. **Finer Grids:** To improve the power of the binary fitting routine, fine mass grids are required. Many isochrone sets include a rough grid of masses along the main sequence. This is visible in the left panel of figure 24. There are very few detected single or binary stars between

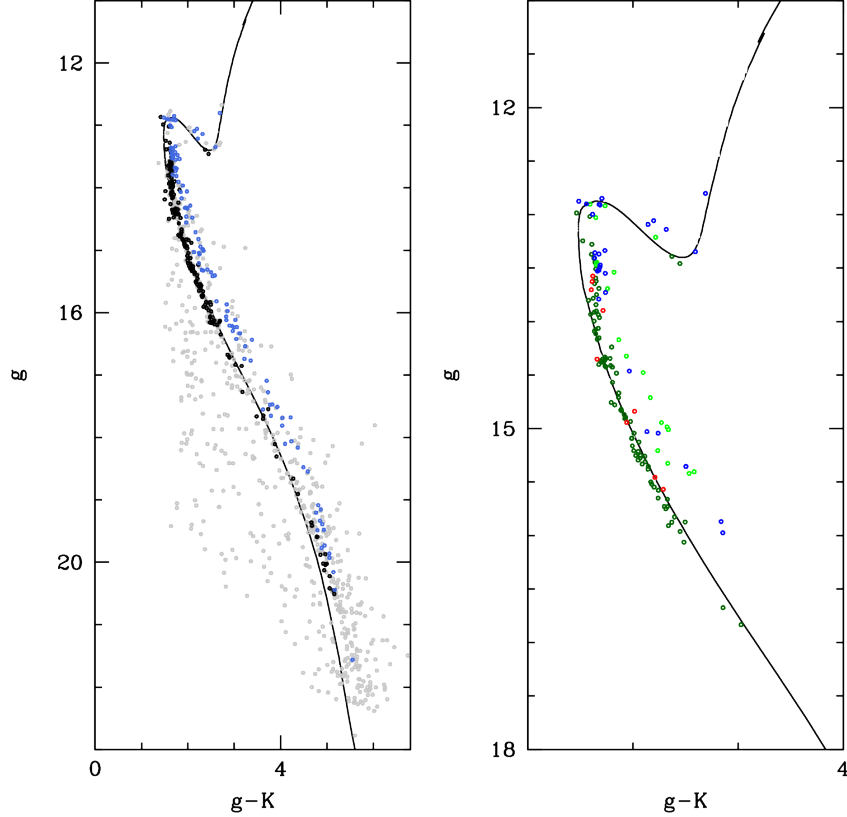


Figure 24: Results of binary fitting on the cluster M67. *Left*: Black = single; blue = binary; grey = too few magnitude values for star. *Right*: Comparison with WOCS RV study. Dark green = both confirmed single; green = both confirmed binary; blue = WOCS single, best-fit binary; red = WOCS binary, best-fit single.

$g \sim 16.5$ and 19 due to the very coarse grid of stellar masses available over this range. We will interpolate the isochrones to create the fine mass grid the fitting routine requires.

3. **Better Isochrones:** The binary fitting routine assumes that the isochrone system being used correctly matches the observational data. The Padova and Dartmouth systems have shown problems in the lower main sequence, leading to inaccurate parameter determination for low-mass systems. Analyzing more isochrone systems, using the technique in 3, will lead to better-fitting isochrone models to use in the binary fitting routine.

References

- An, D., Terndrup, D. M., Pinsonneault, M. H., et al. 2006, arXiv.org, astro-ph, 233
- An, D., Pinsonneault, M. H., Masseron, T., et al. 2009, *The Astrophysical Journal*, 700, 523
- Balaguer-Núñez, L., Jordi, C., Galadí-Enríquez, D., & Zhao, J. L. 2004, *Astronomy and Astrophysics*, 426, 819
- Barmby, P., & Huchra, J. P. 2001, arXiv.org, astro-ph, 2458
- Benjamin, R. A., Churchwell, E., Babler, B. L., et al. 2003, arXiv.org, astro-ph, 953
- Bessell, M. S. 1990, *Astronomical Society of the Pacific*, 102, 1181
- Binney, J., & Merrifield, M. 1998, *Galactic Astronomy* (Princeton University Press)
- Cardelli, J. A., Clayton, G. C., & Mathis, J. S. 1989, *Astrophysical Journal*, 345, 245
- Carney, B. W., Lee, J.-W., & Dodson, B. 2005, *The Astronomical Journal*, 129, 656
- Carroll, B. W., & Ostlie, D. A. 2006, *Introduction to Modern Astrophysics*, 2nd edn.
- Castelli, F., & Kurucz, R. L. 2004, arXiv.org, astro-ph, 5087
- Demarque, P., Woo, J.-H., Kim, Y.-C., & Yi, S. 2004, arXiv.org, astro-ph, 261
- Dias, W. S., Alessi, B. S., Moitinho, A., & Lépine, J. R. D. 2002, *Astronomy and Astrophysics*, 389, 871
- Dotter, A., Chaboyer, B., Jevremovic, D., et al. 2007, *Astrophysical Journal*, astro-ph
- Fan, X. 1999, *The Astronomical Journal*, 117, 2528
- Fazio, G. G., Hora, J. L., Allen, L. E., et al. 2004, *The Astrophysical Journal Supplement Series*, 154, 10
- Fukugita, M., Ichikawa, T., Gunn, J. E., et al. 1996, *Astronomical Journal* v.111, 111, 1748
- Geisler, D., Villanova, S., Carraro, G., et al. 2012, arXiv.org, astro-ph.GA, 3328
- Geller, A. M., & Mathieu, R. D. 2011, *Nature*, 478, 356
- Geller, A. M., Mathieu, R. D., Braden, E. K., et al. 2010, *The Astronomical Journal*, 139, 1383
- Geller, A. M., Mathieu, R. D., Harris, H. C., & McClure, R. D. 2008, *The Astronomical Journal*, 135, 2264
- Girardi, L., Bertelli, G., Bressan, A., et al. 2002, arXiv.org, astro-ph, 195
- Gozzoli, E., Tosi, M., Marconi, G., & Bragaglia, A. 1996, arXiv.org, astro-ph
- Grocholski, A. J., & Sarajedini, A. 2003, arXiv.org, astro-ph

- Hole, K. T., Geller, A. M., Mathieu, R. D., et al. 2009, *The Astronomical Journal*, 138, 159
- Hurley, J., & Tout, C. A. 1998, arXiv.org, astro-ph
- Iglesias, C. A., & Rogers, F. J. 1996, *Astrophysical Journal* v.464, 464, 943
- Mathieu, R. D., Latham, D. W., & Milone, A. E. 1997, *The Third Pacific Rim Conference on Recent Development on Binary Star Research*. Proceedings of a conference sponsored by Chiang Mai University, 130, 113
- Milone, A. P., Piotto, G., Bedin, L. R., et al. 2011, arXiv.org, 1111, 552
- Piotto, G., Bedin, L. R., Anderson, J., et al. 2007, arXiv.org, astro-ph, L53
- Platais, I., Kozhurina-Platais, V., Mathieu, R. D., Girard, T. M., & van Altena, W. F. 2003, *The Astronomical Journal*, 126, 2922
- Skrutskie, M. F., Cutri, R. M., Stiening, R., et al. 2006, *The Astronomical Journal*, 131, 1163
- Stetson, P. B. 1987, *Astronomical Society of the Pacific*, 99, 191
- Stetson, P. B., McClure, R. D., & VandenBerg, D. A. 2004, *The Publications of the Astronomical Society of the Pacific*, 116, 1012
- VandenBerg, D. A., Bergbusch, P. A., Dotter, A., et al. 2012, arXiv.org, astro-ph.SR
- VandenBerg, D. A., Bergbusch, P. A., & Dowler, P. D. 2006, *The Astrophysical Journal Supplement Series*, 162, 375
- von Hippel, T., & Sarajedini, A. 1998, *The Astronomical Journal*, 116, 1789
- Yadav, R. K. S., Bedin, L. R., Piotto, G., et al. 2008, *Astronomy and Astrophysics*, 484, 609